



**HAL**  
open science

## The representation of sea salt aerosols and their role in polar climate within CMIP6

Rémy Lapere, Jennie L Thomas, Louis Marelle, Annica M L Ekman, Markus Michael Frey, Marianne Tronstad Lund, Risto Makkonen, Ananth Ranjithkumar, Matthew Edward Salter, Bjørn Hallvard Samset, et al.

► **To cite this version:**

Rémy Lapere, Jennie L Thomas, Louis Marelle, Annica M L Ekman, Markus Michael Frey, et al.. The representation of sea salt aerosols and their role in polar climate within CMIP6. 2023. hal-04277633

**HAL Id: hal-04277633**

**<https://hal.science/hal-04277633>**

Preprint submitted on 9 Nov 2023

**HAL** is a multi-disciplinary open access archive for the deposit and dissemination of scientific research documents, whether they are published or not. The documents may come from teaching and research institutions in France or abroad, or from public or private research centers.

L'archive ouverte pluridisciplinaire **HAL**, est destinée au dépôt et à la diffusion de documents scientifiques de niveau recherche, publiés ou non, émanant des établissements d'enseignement et de recherche français ou étrangers, des laboratoires publics ou privés.

# The representation of sea salt aerosols and their role in polar climate within CMIP6

Rémy Lapere<sup>1</sup>, Jennie L Thomas<sup>1</sup>, Louis Marelle<sup>2</sup>, Annica M. L. Ekman<sup>3</sup>, Markus Michael Frey<sup>4</sup>, Marianne Tronstad Lund<sup>5</sup>, Risto Makkonen<sup>6</sup>, Ananth Ranjithkumar<sup>4</sup>, Matthew Edward Salter<sup>3</sup>, Bjørn Hallvard Samset<sup>5</sup>, Michael Schulz<sup>7</sup>, Larisa Sogacheva<sup>6</sup>, Xin Yang<sup>4</sup>, and Paul Zieger<sup>3</sup>

<sup>1</sup>Univ. Grenoble Alpes, CNRS, IRD, Grenoble INP, IGE, 38000 Grenoble, France

<sup>2</sup>LATMOS/IPSL, Sorbonne Université, UVSQ, CNRS, Paris, France

<sup>3</sup>Department of Meteorology, Stockholm University, Stockholm, Sweden

<sup>4</sup>Natural Environment Research Council, British Antarctic Survey, Cambridge, UK

<sup>5</sup>CICERO Center for International Climate Research, Oslo, Norway

<sup>6</sup>Finnish Meteorological Institute, Climate Research Programme, Helsinki, Finland

<sup>7</sup>Norwegian Meteorological Institute, Oslo, Norway

December 7, 2022

## Abstract

Natural aerosols and their interactions with clouds remain an important uncertainty within climate models, especially at the poles. Here, we study the behavior of sea salt aerosols (SSaer) in the Arctic and Antarctic within 12 climate models from CMIP6. We investigate the driving factors that control SSaer abundances and show large differences based on the choice of the source function, and the representation of aerosol processes in the atmosphere. Close to the poles, the CMIP6 models do not match observed seasonal cycles of surface concentrations, likely due to the absence of wintertime SSaer sources such as blowing snow. Further away from the poles, simulated concentrations have the correct seasonality, but have a positive mean bias of up to one order of magnitude. SSaer optical depth is derived from the MODIS data and compared to modeled values, revealing good agreement, except for winter months. Better agreement for AOD than surface concentration may indicate a need for improving the vertical distribution, the size distribution and/or hygroscopicity of modeled polar SSaer. Source functions used in CMIP6 emit very different numbers of small SSaer, potentially exacerbating cloud-aerosol interaction uncertainties in these remote regions. For future climate scenarios SSP126 and SSP585, we show that SSaer concentrations increase at both poles at the end of the 21st century, with more than two times mid-20th century values in the Arctic. The pre-industrial climate CMIP6 experiments suggest there is a large uncertainty in the polar radiative budget due to SSaer.

# The representation of sea salt aerosols and their role in polar climate within CMIP6

Rémy Lapere<sup>1</sup>, Jennie L. Thomas<sup>1</sup>, Louis Marelle<sup>2</sup>, Annica M. L. Ekman<sup>3,4</sup>,  
Markus M. Frey<sup>5</sup>, Marianne Tronstad Lund<sup>6</sup>, Risto Makkonen<sup>7</sup>, Ananth  
Ranjithkumar<sup>5</sup>, Matthew E. Salter<sup>3,8</sup>, Bjørn Hallvard Samset<sup>6</sup>, Michael  
Schulz<sup>9</sup>, Larisa Sogacheva<sup>7</sup>, Xin Yang<sup>5</sup>, Paul Zieger<sup>3,8</sup>

<sup>1</sup>Univ. Grenoble Alpes, CNRS, IRD, Grenoble INP\*, IGE, 38000 Grenoble, France

<sup>2</sup>LATMOS/IPSL, Sorbonne Université, UVSQ, CNRS, Paris, France

<sup>3</sup>Department of Meteorology, Stockholm University, Stockholm, Sweden

<sup>4</sup>Bolin Center for Climate Research, Stockholm, Sweden

<sup>5</sup>Natural Environment Research Council, British Antarctic Survey, Cambridge, UK

<sup>6</sup>CICERO Center for International Climate Research, Oslo, Norway

<sup>7</sup>Finnish Meteorological Institute, Climate Research Programme, Helsinki, Finland

<sup>8</sup>Department of Environmental Science, Stockholm University, Stockholm, Sweden

<sup>9</sup>Norwegian Meteorological Institute, Oslo, Norway

\*Institute of Engineering and Management Univ. Grenoble Alpes

## Key Points:

- CMIP6 models have a large uncertainty in present day sea salt aerosol abundance at the poles
- Model performance is degraded closer to the poles suggesting inadequate emissions sources within the polar regions
- Both present and future radiative balance at the poles is uncertain because of sea salt aerosols

---

Corresponding author: Rémy Lapere, [remy.lapere@univ-grenoble-alpes.fr](mailto:remy.lapere@univ-grenoble-alpes.fr)

Corresponding author: Jennie L. Thomas, [jennie.thomas@univ-grenoble-alpes.fr](mailto:jennie.thomas@univ-grenoble-alpes.fr)

## Abstract

Natural aerosols and their interactions with clouds remain an important uncertainty within climate models, especially at the poles. Here, we study the behavior of sea salt aerosols (SSaer) in the Arctic and Antarctic within 12 climate models from CMIP6. We investigate the driving factors that control SSaer abundances and show large differences based on the choice of the source function, and the representation of aerosol processes in the atmosphere. Close to the poles, the CMIP6 models do not match observed seasonal cycles of surface concentrations, likely due to the absence of wintertime SSaer sources such as blowing snow. Further away from the poles, simulated concentrations have the correct seasonality, but have a positive mean bias of up to one order of magnitude. SSaer optical depth is derived from the MODIS data and compared to modeled values, revealing good agreement, except for winter months. Better agreement for AOD than surface concentration may indicate a need for improving the vertical distribution, the size distribution and/or hygroscopicity of modeled polar SSaer. Source functions used in CMIP6 emit very different numbers of small SSaer, potentially exacerbating cloud-aerosol interaction uncertainties in these remote regions. For future climate scenarios SSP126 and SSP585, we show that SSaer concentrations increase at both poles at the end of the 21<sup>st</sup> century, with more than two times mid-20<sup>th</sup> century values in the Arctic. The pre-industrial climate CMIP6 experiments suggest there is a large uncertainty in the polar radiative budget due to SSaer.

## 1 Introduction

The polar regions have a larger sensitivity to changes in global climate than any other region (Manabe & Wetherald, 1975; Meredith et al., 2019). This is called polar amplification, which refers to the multiple factors that control why polar regions are changing faster than the rest of the planet. A key reason for polar amplification is sea ice and snow loss, which changes surface albedo from light to dark and induces an additional regional warming, or climate feedback (Hall, 2004). Atmospheric temperature feedbacks such as the Planck feedback and local lapse-rate feedback also play an important role in this amplification (Stuecker et al., 2018). Rantanen et al. (2022) found that climate models and observational data disagree on the magnitude of Arctic amplification over the past 40 years, with larger trends found in observations. Climate models capture some aspects of polar amplification, but not all of the complexity of what is occurring within the rapidly changing polar regions, in particular in the Antarctic where the model bias is even more pronounced (D. M. Smith et al., 2019).

Clouds are a key, uncertain component of the polar and global climate system (Flato et al., 2013). Specifically, clouds can have both a cooling (via reflection of shortwave radiation) and warming (by trapping longwave radiation) effect on the polar atmosphere, depending on their optical thickness and cloud droplet number as reviewed in Alkama et al. (2020). As a result, polar clouds in summer have the potential to dampen the radiative impact of sea ice loss through shortwave cooling (Alkama et al., 2020), but summertime low-level clouds in the Arctic can also favor sea ice melt through longwave warming (Y. Huang et al., 2021). In wintertime, the surface cloud forcing at the poles is stronger than in summer and with a warming effect (Curry et al., 1996).

Aerosols are also a key uncertainty in climate models globally and have even larger uncertainties in the polar regions (Sand et al., 2017). Aerosols influence the climate through their interaction with radiation directly (aerosol direct effect) and their role in cloud formation/modification (aerosol indirect and semi-direct effects) (Myhre et al., 2013). Natural sources of aerosols and their impacts on clouds have been less of a focus than understanding anthropogenic aerosols and their direct and indirect radiative effects (Schmale et al., 2021; Boucher et al., 2013; Sand et al., 2021; Samset, 2022). However, it is challenging to separate the effects on clouds and radiation of anthropogenic and natural aerosols,

75 and these effects can have opposite signs, including at the poles (Allen & Sherwood, 2011).  
76 In addition, cloud-aerosol interactions are non-linear (Gryspeerd et al., 2019), so esti-  
77 mating anthropogenic impacts on polar clouds requires an accurate understanding of the  
78 natural aerosol baseline. Therefore improved representation of natural aerosols and their  
79 impacts on clouds are essential for improved anthropogenic climate change estimates.

80 Sea salt particles resulting from sea spray make up most of the aerosol mass over  
81 oceanic regions (Andreae & Rosenfeld, 2008), with an even larger fraction over the pol-  
82 ar regions (Sand et al., 2017). Sea spray is composed of a mixture of inorganic salts and  
83 an organic fraction (including both dissolved organics and fragments of organic mate-  
84 rial). In this study, we focus on the inorganic fraction of sea spray emissions and use the  
85 wording sea salt aerosols (SSaer) to refer to the inorganic fraction (sodium chloride, sul-  
86 fate, and other trace salt species) of sea spray. When discussing sea spray we refer to the  
87 full mixture of emitted species, which includes both inorganic and organic marine aerosols.

88 SSaer and sulfate emitted from sea spray can act as Cloud Condensation Nuclei  
89 (CCN) (Prank et al., 2022; Xu et al., 2022), and marine organics can act as Ice Nucle-  
90 ating Particles (INP) (Wilson et al., 2015; DeMott et al., 2016). Over polar oceans, sea  
91 spray aerosols including SSaer can seasonally make up most of the cloud seeding pop-  
92 ulation (Quinn et al., 2017; Fossum et al., 2018). They also scatter incoming solar short-  
93 wave radiation directly (Takemura et al., 2002; Satheesh & Lubin, 2003). In addition,  
94 SSaer also change the climate impacts of other species, including anthropogenic pollu-  
95 tants such as nitrate (Chen et al., 2020) and sulfate (Fossum et al., 2020), by regulat-  
96 ing their droplet activation. Furthermore, SSaer modulate polar atmospheric chemistry  
97 by providing a surface for heterogeneous reactions and leading to bromine activation, with  
98 major effects on ozone and mercury depletion events (Hara et al., 2018; Zhu et al., 2019;  
99 Marelle et al., 2021). Accurately modeling sea spray aerosols, including inorganic SSaer,  
100 is therefore a prerequisite for properly representing the polar atmosphere. In particu-  
101 lar, the SSaer physical parameters key to their cloud and radiation interaction and re-  
102 moval processes, are the number flux, the size distribution, and the hygroscopicity.

103 Sea spray emission over the open ocean is due to wind action that forms bursting  
104 bubbles at the sea surface, visible as white caps, which emit aerosols to the atmosphere  
105 (Monahan et al., 1986). The sea surface temperature (SST) can also modulate the size  
106 and number of aerosols emitted (Mårtensson et al., 2003; Jaeglé et al., 2011; Salter et  
107 al., 2015; Liu et al., 2021). Salinity affects the electrolytic properties of water, and as salin-  
108 ity increases, coalescence is inhibited and bubbles form in larger number and smaller radii,  
109 which then also affects the emission flux of SSaer (Zinke et al., 2022). There remain sig-  
110 nificant uncertainties in the open ocean sourced sea spray aerosol emission fluxes, includ-  
111 ing the relatively well-studied inorganic SSaer, that is emitted into the atmosphere, espe-  
112 cially at the cold temperatures in the polar regions. For example, Regayre et al. (2020)  
113 found that sea spray emissions in the Southern Ocean needed to be tripled in a global  
114 simulation to match observations. Unlike other oceanic areas in the world that remain  
115 open throughout the year, estimates of sea spray emissions at the poles depend on a proper  
116 representation of sea ice cover, which is still challenging in climate models and exhibits  
117 a large spread in model ensembles (Notz & SIMIP Community, 2020; Roach et al., 2020).  
118 Additional polar-specific source processes of SSaer include blowing snow over sea ice (Yang  
119 et al., 2008; J. Huang & Jaeglé, 2017; Yang et al., 2019; Marelle et al., 2021) and emis-  
120 sion fluxes specific to open water leads (Held et al., 2011; Kirpes et al., 2019; Ioannidis  
121 et al., 2022). Climate models parameterize emissions from open water leads in sea ice  
122 like those from the open ocean, even though wave action and white caps are very dif-  
123 ferent in leads than in open ocean due to e.g., reduced wind fetch, local convection, and  
124 the lack of a surf zone on the sea-ice edge (Nilsson et al., 2001). Blowing snow sources  
125 of SSaer on the other hand are usually not included in global models and to our knowl-  
126 edge are not included in CMIP6 models.

127 Due to the ongoing trend of sea ice retreat (Meredith et al., 2019), sea spray emis-  
 128 sions at the poles are likely to increase in the coming decades. Specifically, less sea ice  
 129 means more open ocean and therefore more sea spray (Struthers et al., 2013). In par-  
 130 allel, increased sea spray emissions probably have a negative effective radiative forcing  
 131 globally (Thornhill et al., 2021), including at the poles (Korhonen et al., 2010; Browse  
 132 et al., 2014), where it is likely dominated by the aerosol-cloud interaction (Struthers et  
 133 al., 2011). The cooling induced by SSAer-cloud interactions could partially compensate  
 134 for the warming caused by sea ice loss. Accurate representation of SSAer in the atmo-  
 135 sphere is also important for reliable future climate projections. However, both AeroCom  
 136 (Sand et al., 2017) and the Coupled Model Intercomparison Project phase 6 (CMIP6)  
 137 (Mortier et al., 2020; Gliš et al., 2021) reported a large uncertainty in the aerosol bud-  
 138 get and seasonality, globally and at the poles. Fanourgakis et al. (2019) also indicated  
 139 significant model diversity of up to two orders of magnitude in simulated SSAer concen-  
 140 trations over the Southern Ocean, resulting from different parameterizations in global  
 141 models.

142 In the present work, we address the following science questions:

- 143 1. How diverse are SSAer emissions/concentrations at the poles in CMIP6 models?
- 144 2. What are the drivers of this model diversity?
- 145 3. How well do the CMIP6 models and ensembles represent SSAer at the poles rel-  
 146 ative to surface observations and remote sensing?
- 147 4. What are the implications of model diversity and changes in SSAer emissions, for  
 148 the present and future polar climate?

149 To answer these questions, we conduct an assessment of polar SSAer diversity in CMIP6  
 150 models in Section 3.1, by comparing SSAer related variables in the CMIP6 historical ex-  
 151 periment. We further evaluate the models against SSAer concentration data from mea-  
 152 surement stations and aerosol optical depth from the Moderate-Resolution Imaging Spec-  
 153 troradiometer (MODIS) Aqua and Terra satellite products in Section 3.2. Finally, in Sec-  
 154 tion 3.3 we analyze the historical and future trends of SSAer in the Shared Socioeconomic  
 155 Pathways 126 and 585 scenarios and the sensitivity of the polar radiative budget to changes  
 156 in SSAer emissions, through different CMIP6 experiments to shed light on the implica-  
 157 tions of modeling discrepancies in CMIP6.

## 158 2 Materials and Methods

### 159 2.1 Models

160 We use results from 12 climate models that are part of CMIP6. Models were se-  
 161 lected based the availability of relevant variables for the evaluation of SSAer. The mod-  
 162 els included, along with the available variables and source function formulation are in-  
 163 dicated in Table 1. Only one additional CMIP6 model features the mass mixing ratio  
 164 of sea salt aerosol variable (*mmrss*) for the historical experiment (INM-CM5). We have  
 165 chosen to discard this model because it produces unrealistic SSAer concentrations that  
 166 are three orders of magnitude larger than any other model. All other CMIP6 models are  
 167 excluded because they do not provide *mmrss* in the historical experiment.

168 In order to evaluate the representation polar SSAer within CMIP6 models, we ex-  
 169 tracted the following from the Earth System Grid Federation (ESGF) platform (ESGF,  
 170 2014), for the historical CMIP6 experiment (run with coupled ocean-atmosphere mod-  
 171 els) and for the period 1951–2014 (as summarized in Table 1): mass mixing ratio of sea  
 172 salt aerosol (*mmrss*), sea salt aerosol emission flux (*emiss*), sea ice concentration (*siconc*),  
 173 surface wind speed (*sfcWind*), optical depth of sea salt aerosol at 550 nm (*od550ss*) and  
 174 planetary boundary layer height (*bldep*). We use this information for all 12 models, but  
 175 exclude variables that were missing as output on the ESGF platform for certain mod-

176 els. Future projections are also considered in this work, relying on the Shared Socio-  
 177 economic Pathway (SSP) 126 and 585 experiments (ScenarioMIP activity - O’Neill et al.  
 178 (2016)). The significance, sign and magnitude of trends in these scenarios are calculated  
 179 using a Mann-Kendall test (Mann, 1945). For the evaluation of SSAer radiative impact,  
 180 two experiments of the AerChemMIP activity are considered. For that, the top-of-atmosphere  
 181 net downward radiation flux (*rtmt*) and near-surface air temperature (*tas*) in experiments  
 182 *piClim-2xss* and *piClim-control* pre-industrial (30 years under 1850 climate) atmospheric  
 183 composition scenarios are investigated.

184 For spatial ensemble means, model output is first re-gridded to a common grid, to  
 185 the lowest model resolution available ( $2^\circ\text{lon}\times 1.5^\circ\text{lat}$ ). The re-gridding is done using Cli-  
 186 mate Data Operators bilinear remapping tool (Schulzweida et al., 2012). For regionally  
 187 averaged numbers, a weighted mean is applied, with weights corresponding to the grid  
 188 cell area. Ground station data usually provide a mass concentration of sodium, whereas  
 189 models output the SSAer mass mixing ratio. For the comparison between the two, the  
 190 SSAer mass mixing ratio is therefore converted into a mass concentration under a stan-  
 191 dard air density at 1 atmosphere and  $0^\circ\text{C}$  temperature ( $1.2922\text{ kg m}^{-3}$ ). SSAer in the mod-  
 192 els is assumed to follow the composition of Seinfeld and Pandis (2016), and sodium mass  
 193 is thus taken as 30.61% of SSAer mass. Near-surface concentration in the models refers  
 194 to the concentration within the lowest vertical level. Furthermore, the atmospheric life-  
 195 time of SSAer is calculated as the global load (that is, the integral of *mvrss* on the ver-  
 196 tical levels for each latitude and longitude) divided by the global emission rate, weighted  
 197 by grid cell area. We do not use deposition for the the lifetime analysis because it is only  
 198 available for 8 out of the 12 models. The metrics used to compare models and observa-  
 199 tions are the normalized mean bias (NMB), defined as  $\text{NMB} = (\bar{j}\text{MODEL}_i - \bar{j}\text{OBS}_i) / \bar{j}\text{OBS}_i$ ,  
 200 where  $\bar{j}_i$  is the annual mean, and the Pearson correlation coefficient, simply referred to  
 201 as correlation (R).

202 Among the 12 models considered, sea spray emissions are parameterized by 8 dif-  
 203 ferent source functions or combinations of source functions (Table 1). The common fea-  
 204 ture of these source functions is that for a given aerosol radius, the emission flux is pro-  
 205 portional to the wind speed raised to a varying exponent. Some of the parameterizations  
 206 also account for the dependence of sea spray emissions on SST. Although there is still  
 207 debate on the exact role that SST plays in the sea spray emission process, including it  
 208 generally improves the fit with observations as reviewed in Grythe et al. (2014). For ex-  
 209 ample, the Jaeglé et al. (2011) parameterization decreases emissions at colder SST, whereas  
 210 the Salter et al. (2015) source function does the opposite. For polar waters, for exam-  
 211 ple, an increase in SST may decrease the number of sea spray aerosol produced, with-  
 212 out significantly affecting the shape of the size distribution (Zábori et al., 2012). This  
 213 is consistent with the Salter et al. (2015) source function, but opposite to the SST de-  
 214 pendence in the Jaeglé et al. (2011) source function, for which emissions increase at higher  
 215 SST. This shows that not all source functions may be fit for use in polar regions. The  
 216 source functions are further investigated in Section 3.1.2 based on offline calculations from  
 217 the source function formulations, using a sectional approach with fixed bins, regardless  
 218 of what is actually done in the models. This approach is used to evidence the diversity  
 219 coming from the source functions themselves rather than the aerosol schemes of the mod-  
 220 els.

221 To our knowledge, polar-specific sources of SSAer such as blowing snow over sea ice  
 222 and emissions from leads are not taken into account in CMIP6 climate models, which  
 223 may limit their performance at high latitudes. Similarly, only the fraction of the ocean  
 224 that is ice-free can lead to sea spray emissions. Therefore, SSAer emissions at the poles  
 225 in climate models are highly dependent on a proper representation of sea ice cover. As  
 226 a consequence, SSAer emissions are probably harder to adequately model at the poles  
 227 than in any other oceanic region in the world. However, even for mid-latitudes and more  
 228 generally globally, climate models disagree on SSAer representation, such as their total

229 emission fluxes, lifetime, burden, and optical properties including hygroscopicity (Burgos  
 230 et al., 2020; Glib et al., 2021). The sinks of SSaer such as dry and wet deposition, con-  
 231 trol their atmospheric quantities. Accurate wet deposition rates require adequate pre-  
 232 cipitation, which is challenging for Antarctica (Roussel et al., 2020) and the Arctic (Diaconescu  
 233 et al., 2018) in climate models. In parallel, dry deposition of aerosols is sensitive to the  
 234 choice of deposition velocity, which is usually not tuned for snow-covered terrain in chemistry-  
 235 transport models, resulting in large uncertainties in the Arctic (Qi et al., 2017). Dry de-  
 236 position is also sensitive to boundary layer stability, which is difficult to model especially  
 237 in polar regions (Holtstag et al., 2013). Finally, the transport of aerosols from the mid-  
 238 latitudes to the poles can also represent a source of uncertainty in the models. There-  
 239 fore, it is not expected that climate models would converge in regions as complex as the  
 240 poles, where in addition to emission fluxes, meteorology (Cai et al., 2021) and anthro-  
 241 pogenic aerosol budgets (Sand et al., 2017) are more challenging to represent.

### 242 **2.1.1 Reanalysis**

243 In order to assess how CMIP6 models compare with more widely used air quality-  
 244 oriented reanalyses, this work includes two monthly reanalysis products. The Modern-  
 245 Era Retrospective analysis for Research and Applications, Version 2 (MERRA2) (Merrill et al.,  
 246 2019) and the Copernicus Atmosphere Monitoring Service (CAMS) (Copernicus, 2019). For the  
 247 former, the Sea Salt Surface Mass Concentration (*SSSMASS*) variable from the *avg1\_2d\_aer\_Nx*  
 248 monthly product is considered, over the period 1980–2021. For the latter, the *CAMS global*  
 249 *reanalysis (EAC4) monthly averaged fields* product is used and the three size bins of the  
 250 *Sea salt aerosol mixing ratio* variable are summed and taken at the first model level, over  
 251 the period 2003–2021. We also use the monthly climatology of sea ice concentration from  
 252 the fifth generation ECMWF atmospheric reanalysis of the global climate (ERA5) (ERA5, 2019).

## 253 **2.2 Observations**

### 254 **2.2.1 Ground based stations**

255 Combining data from the literature (Legrand et al., 2016; Yang et al., 2019) and  
 256 from the EBAS platform (Norwegian Institute for Air Research, 2022), sodium aerosol  
 257 concentration measurements were obtained over a multiyear period for 9 stations in the  
 258 Arctic and 5 in the Antarctic. Their location, the data source, and the period covered  
 259 by the observations are detailed in Figure 1. When taken from the EBAS platform, the  
 260 weekly measurements of atmospheric sodium, typically conducted using high-volume air  
 261 samplers, are then averaged to obtain the annual cycle of monthly means and the related  
 262 standard deviations, over the entire time period in the data set. We use these observa-  
 263 tions without assuming a particular cut-off size and directly compare to the total sodium  
 264 mass derived from the modeled SSaer (maximum radii in the models can be found in Ta-  
 265 ble 1).

266 The nine Arctic stations include two sites above 80°N (Alert and Villum) in Canada  
 267 and Greenland, respectively. These two coastal sites are surrounded by sea ice even in  
 268 summer (blue contour in Figure 1). Data from a third coastal site (Utqiagvik, Alaska,  
 269 71°N) is available, where, in contrast to Alert and Villum, the shore is sea ice free in sum-  
 270 mer but sea ice covered in winter. Summit (Greenland) is an inland station in the mid-  
 271 dle of Greenland. Zeppelin (Svalbard) is a mountainous site (475 m a.s.l.) near the shore  
 272 of a fjord at 79°N, which is more and more influenced by sea spray (Heslin-Rees et al.,  
 273 2020). The rest of the Arctic stations considered in this work are in northern Europe (Irafoss  
 274 in Iceland, Pallas in Finland, Karasjok in Norway and Breckälén in Sweden). For Antarc-  
 275 tica, one of the five stations is far inland (Concordia), one is on the coast of East Antarc-  
 276 tica (Dumont d’Urville) and the three others are in coastal western Antarctica (Halley,  
 277 Neumayer, Palmer). These stations are located between 65°S and 75°S (Figure 1).



278

### 2.2.2 Satellite remote sensing

279

280

281

282

283

284

285

286

287

288

289

290

A regional evaluation of SSAer in CMIP6 is conducted by comparing its modeled optical depth with aerosol optical depth (AOD) satellite data from MODIS (Platnick, 2015). To our knowledge, there is no pure satellite climatology for SSAer AOD. Those products available such as MACv2 (Kinne, 2019) usually include a modeled component in their climatology. For the purpose of this CMIP6 model evaluation, a proxy based on MODIS AOD and Angstrom exponent is therefore used to create a simple version of this missing product. A more refined dedicated polar marine AOD climatology product could be created by combining several satellite sources (Dror et al., 2018; Dasarathy et al., 2021; Atmoko & Lin, 2022) in future work. However, the Arctic time series obtained using the methodology described below (Section 3.2.2) is well in line with the SSAer AOD values reported in Xian et al. (2022) for example, which are based on an ensemble of reanalyses. This suggests that the simple proxy used here yields reasonable values of SSAer AOD.

291

292

293

294

295

296

297

298

299

300

301

302

303

304

305

306

307

308

309

310

This custom product is based on the MODIS Atmosphere L3 Monthly Products MOD08\_M3 (from satellite Terra) and MYD08\_M3 (from satellite Aqua) (Platnick, 2015) for the period 2005–2014. The monthly mean AOD at 550 nm is taken from the Dark Target/Deep Blue (DTDB) combined variable *AOD\_550\_Dark\_Target\_Deep\_Blue\_Combined\_Mean\_Mean*. Then, a filter is applied that aims at keeping only the contribution of SSAer to AOD. This filter is based on the condition that the Angstrom exponent is below 1 to filter out fine-mode aerosols. The implied assumptions are that SSAer are dominated by coarse-mode particles and that coarse-mode aerosols over the polar oceans are dominated by SSAer. The former is shown in e.g. Murphy et al. (2019), the latter assumption is discussed in the next paragraph. The *Aerosol\_AE1\_Ocean\_JHisto\_vs\_Opt\_Depth* variable from MOD08\_M3 and MYD08\_M3 is used to discriminate Angstrom exponents. It contains, for each month and grid cell, a joint histogram of the calculated Angstrom exponent (0.55–0.86  $\mu\text{m}$ ) versus retrieved AOD at 550 nm. This variable provides data only over oceans, and as a result the product we build here is only valid for oceans. We use it as follows: for each grid cell and month, the frequency of records with  $AE < 1$  i.e.  $\text{Freq}_{AE < 1} = \text{Counts}_{AE < 1} / \text{Counts}_{SAE}$  is computed, regardless of the AOD joint distribution. The DTDB 550 nm AOD is then multiplied by this  $\text{Freq}_{AE < 1}$  factor to approximate the fraction of AOD attributable to coarse-mode aerosols, and by extension SSAer. The resulting estimated fraction of AOD from MODIS attributed to SSAer is referred to as AOD<sub>ss</sub> in the continuation. The algorithm created to build this AOD<sub>ss</sub> extraction from MODIS is attached to this paper.

311

312

313

314

315

316

317

318

319

320

321

322

323

324

325

326

327

The key assumption for the validity of this approach is that coarse-mode aerosols in the MODIS records are dominated by SSAer over polar oceans and therefore that dust has a minor contribution. This hypothesis is supported by the MACv2 aerosol climatology (Kinne, 2019), which provides AOD based on AERONET/MAN and climate models, with species differentiation. We use this data set to evaluate the contribution of SSAer AOD to {SSaer+dust} AOD and assess the validity of the assumption that dust is not an important fraction. In this data set, the fraction of {SSaer+dust} AOD attributed to SSAer is well above 80% over most of the polar oceans, except in coastal areas where important dust sources can be found (Meinander et al., 2022) and the central Arctic, which is permanently covered with sea ice (Figure 1). For these regions, however, AOD in MACv2 is very low and/or dominated by the fine-mode fraction, which is filtered out by our Angstrom exponent criterion. Therefore the MACv2 product supports the assumption that coarse-mode AOD over the polar oceans is essentially SSAer AOD, as illustrated in Figure A1. Sporadic transport events of aerosols (volcanic ash, biomass burning, anthropogenic pollution) can also affect the signal recorded by MODIS, but we argue that such short-lived events are smoothed out by the monthly averaging, except where the number of available records is low.

### 3 Results and discussion

#### 3.1 Representation of polar SSAer in CMIP6

In the Arctic, the CMIP6 1951–2014 climatology of the SSAer surface mass mixing ratio (referred to as *mmrss* from now on) shows maximum values over the northern Atlantic and northern Pacific (Figure 2), with the mixing ratio decreasing poleward, reaching averages below  $1 \mu\text{g kg}^{-1}$  in the high Arctic. CNRM-ESM is an exception, with mixing ratios more than one order of magnitude greater than any other model. This discrepancy is discussed later on. The northward negative gradient is consistent with an increase of the relative area fraction covered by sea ice as latitudes increase, which inhibits the production of sea spray. Over the continents, concentrations are generally below  $1 \mu\text{g kg}^{-1}$ , down to less than  $50 \text{ ng kg}^{-1}$  in some models, with *mmrss* decreasing inland, in connection with the deposition of the SSAer during transport. Therefore, all the models have characteristics that are consistent with the expected behavior of SSAer production and transport patterns.

Although the spatial distribution remains relatively consistent (Figure 2), in terms of magnitude, there is a large diversity between models. CNRM-ESM appears as an outlier at both poles, yielding very high *mmrss* of up to  $900 \mu\text{g kg}^{-1}$ , 20 times larger than any other model. This can be explained by a larger coarse size radius of SSAer at emission in CNRM-ESM compared to the other models, as already noted in Thornhill et al. (2021). In this regard, CNRM-ESM being an outlier, this model is not included in the continuation of the analysis unless explicitly mentioned. CNRM-ESM aside, GISS presents the highest mixing ratios, with more than  $40 \mu\text{g kg}^{-1}$  in the northern Atlantic and more than  $1 \mu\text{g kg}^{-1}$  over most of the high Arctic and continental areas. At the other end of the spectrum, MRI-ESM and MIROC-ES2L do not exhibit mixing ratios above  $10 \mu\text{g kg}^{-1}$ , and they drop to less than  $50 \text{ ng kg}^{-1}$  over continental areas. This spread in magnitudes will be further analyzed in Section 3.1.2 based on source functions. In some models, the latitudinal gradients are sharper (e.g. BCC-ESM compared to EC-Earth) suggesting different representations of atmospheric dynamics (transport, boundary layer dynamics) and deposition (dry and wet).

For the Antarctic (Figure 3), this climatology of *mmrss* has larger values than for the Arctic, due to the Southern Ocean providing a large source area of sea spray combined with strong winds. A band of maximum *mmrss* is found around  $50^\circ\text{S}$  in the Southern Ocean in all the models, followed by a negative gradient toward the pole related to deposition during the transport. Again, CNRM-ESM aside, GISS presents the highest values, whereas MRI-ESM and MIROC-ES2L have the lowest, and the poleward gradient is more or less sharp depending on the model. Similarly to the Arctic, CMIP6 models give a generally consistent spatial distribution of *mmrss* in the Antarctic, except for the magnitudes, which are even more diverse.

The diversity in spatial gradients between models is particularly relevant for the interpretation of ice cores from polar ice sheets (Greenland, Antarctica). Sea salt in ice cores at coastal sites can be used as a proxy for sea ice conditions variability, but models usually show that for continental polar areas, meteorology, atmospheric transport, and deposition control sea salt in ice cores instead (Levine et al., 2014; Rhodes et al., 2018). The differences in transport shown here in CMIP6 models suggest that the relative attribution of sea salt variability in ice cores to transport meteorology and changes in the sea ice source can be quite uncertain. The spatial distribution is consistent from one model to another, but differences in gradient suggest that the representation of atmospheric dynamics and sinks (wet and dry deposition) may differ.

Figure 4 further summarizes the model diversity, including for other SSAer related variables. Similarly to mixing ratios, there is a large diversity in total mass emission and deposition fluxes, which partly accounts for the diversity in *mmrss*. In addition, SSAer

379 are not found at the same altitudes in all the models. This information is contained in  
 380 the aerosol layer height, which is defined as a weighted mean of SSAer layer height us-  
 381 ing the *mmrss* of each layer as the weight (Figure 4). For CESM this height is 956 m,  
 382 while it is only 136 m in IPSL-CM6. This aerosol layer height is important when it comes  
 383 to the interaction of SSAer with clouds. The residence time (or lifetime) of SSAer is one  
 384 of the most diverse metric, with values between a few hours up to several days depend-  
 385 ing on the model. This factor may explain the differences in transport over land, since  
 386 models with longer residence time also feature higher concentrations over Antarctica and  
 387 Greenland (Figures 2 and 3). These differences in lifetime can be explained by the ver-  
 388 tical distribution of SSAer: models with longer lifetime also have higher aerosol layer height.  
 389 GISS is an exception in that case, but the relatively small deposition flux compared to  
 390 the other models compensates for the lower aerosol height and extends the residence time.  
 391 SSAer optical depth is also diversely represented in the models, and not directly related  
 392 to *mmrss*, indicating possible differences in the parameterizations of the size distribu-  
 393 tion and hygroscopicity. We note that the GISS AOD values for SSAer are much higher  
 394 than other models, therefore we exclude this model from the AOD analysis that follows.

395 In summary, there is a large diversity in CMIP6 models in terms of their SSAer cli-  
 396 matologies at the poles, from the mass emissions (factor 3 between lower and higher mod-  
 397 els) to the surface mass mixing ratios (factor 4-5), through the aerosol layer height (fac-  
 398 tor 7-8), lifetime (factor 9), optical depth (factor 4) and total deposition (factor 2-3). In  
 399 the Arctic, dry deposition is more diverse (factor 15) than wet deposition (factor 3), whereas  
 400 in the Antarctic, both dry and wet deposition have a similar inter-model spread (factor  
 401 9). This difference in variability in wet deposition might be related to the difficulty to  
 402 properly reproduce Antarctic precipitation in models (Palerme et al., 2017).

### 403 **3.1.1 Model diversity drivers**

404 The diversity in SSAer climatology is further investigated and explained in terms  
 405 of the annual cycle of *mmrss* and the associated drivers (Figure 5). *mmrss* over the ocean  
 406 is driven by emissions, the height of the boundary layer, and deposition rates. Emissions  
 407 are themselves driven by wind speed and sea ice fraction. SST also affects emissions, but  
 408 for consistency this variable is not included in the following analysis on annual cycles of  
 409 emission drivers, since only four of the models take it into account in their source func-  
 410 tion. Here the focus is on the dynamical drivers and their effects on emissions and con-  
 411 centrations. Figure 5 presents the annual cycle of the aforementioned variables for the  
 412 Arctic and Antarctic, averaged over grid points where emissions are strictly positive and  
 413 the open ocean fraction is at least 10%. This filter is applied to allow a fair comparison  
 414 across all models.

415 In the Arctic, mass emissions are consistently at their lowest in the summer months  
 416 (Figure 5c), when despite increasing sea ice melt and therefore increasing open ocean area  
 417 (Figure 5e), wind speeds are at their lowest (Figure 5g), thus limiting sea spray. All mod-  
 418 els show similar magnitudes in summer, except for IPSL-CM6 which features greater val-  
 419 ues. The spread is larger in the fall/winter months with a factor of up to three between  
 420 IPSL-CM6 and GISS on the total emission rate in October. This diversity in emissions  
 421 seems driven mainly by diversity in sea ice (larger spread) and then by wind speed. Fur-  
 422 thermore, the source function formulation and size distribution of the emitted aerosols  
 423 are key factors that are discussed in Section 3.1.2.

424 For the winter months, when wind speeds are higher, the sea ice fraction seems to  
 425 be the factor limiting emissions, while in the fall, when there is more open ocean, the  
 426 wind seems to be the controlling factor. In parallel, the ongoing reduction of sea ice cover  
 427 in the Arctic appears to be correlated with stronger winds in fall/winter months (Vavrus  
 428 & Alkama, 2022). Therefore, in the context of future climate, the shape of the annual  
 429 cycle of emissions is likely to change, with possibly an even greater amplitude between

430 summer and fall/winter emissions. Given that the radiative impact of SSAer changes with  
 431 seasons (Section 3.3.1), changes in the seasonality of SSAer emissions might have impor-  
 432 tant implications for the polar climate.

433 For the Antarctic (Figures 5d, f, h), the emission drivers are even more spread across  
 434 models, particularly the open ocean fraction in the winter months, resulting in a diver-  
 435 sity factor of up to 6 in total mass emissions. Unlike for the Arctic, annual cycles show  
 436 different shapes in some models. For example, MIROC-ES2L and MPI-ESM show a SSAer  
 437 production peak in May–Jun whereas the other models have maximum emissions in Mar–  
 438 Apr, along with a sharper seasonality. In this case, the sea ice cover appears to be the  
 439 reason for this diversity.

440 The diversity in emissions is partly translated into *mmrss* (Figure 5a, b) although  
 441 it does not account for the relative ranking of the models or for some characteristics of  
 442 the annual cycle. For example, GISS is the model with the lowest mass emissions in the  
 443 Arctic (Figure 5c), and around median emissions in the Antarctic (Figure 5d), but shows  
 444 the highest mixing ratios at both poles. This could result from the representation of the  
 445 dynamics of the boundary layer, since GISS has a mean planetary boundary layer height  
 446 between 300 to 500 m, about three times lower than other models (Figure 5i, j), which  
 447 results in a higher boundary layer concentration for the same amount of emissions. EC-  
 448 Earth also shows very shallow boundary layer heights similar to those of GISS, along with  
 449 a comparatively higher emission rate at both poles, which should result in mixing ratios  
 450 higher than in the other models. However, those mixing ratios are lower, due to a shorter  
 451 lifetime of SSAer of around 14 h, while it is more than a day in GISS (Figure 4). This  
 452 is also reflected by a deposition flux twice as large in EC-Earth compared to GISS, where  
 453 the difference mostly comes from dry deposition (Figure 4). In terms of the annual cy-  
 454 cle, in the Arctic the seasonality of the boundary layer height shows the same shape as  
 455 for emissions, which are both consistent across models. Therefore, the cycle of mixing  
 456 ratio follows the cycle of emissions. However, in the Antarctic, the planetary boundary  
 457 layer height cycle is more diverse, as is the case for emissions, resulting in more diverse  
 458 values and seasonality. Deposition fluxes and lifetimes further modify the relative rank-  
 459 ing of models in terms of mixing ratio as shown in Figure 4, but the seasonality is not  
 460 affected.

### 461 3.1.2 Role of emission source functions

462 The source function formulations also affect the diversity in emissions. Figure 6 ex-  
 463 plores the differences in fluxes resulting from the diversity of source functions used in  
 464 the CMIP6 models. The source functions and aerosol modes/bins used in the models are  
 465 summarized in Table 1. All the models except NorESM use a whitecap fraction approach  
 466 based on surface wind speed, but not all include a dependence on SST. Instead, NorESM  
 467 uses the air-entrainment-based Salter et al. (2015) formulation.

468 Figure 6a shows the theoretical mass flux from an offline calculation of SSAer emis-  
 469 sions for each source function using an arbitrary fixed wind speed and SST ( $10 \text{ m s}^{-1}$  and  
 470  $5^\circ\text{C}$ , respectively) and varying aerosol size bins, as described in Section 2.1. Figure 6b  
 471 explores the effect on this flux of varying wind speed and SST for given size bins. Some  
 472 CMIP6 models use a modal aerosol approach, some use a sectional (size bins) aerosol  
 473 approach. Here, for the sake of comparability of the source functions, we use a sectional  
 474 approach for the aerosol sizes. Therefore, the following analysis reflects the model di-  
 475 versity due to the source functions without considering the actual aerosol size distribu-  
 476 tions (modal or sectional) that are included within each model.

477 Figures 2 and 3 show that CNRM-ESM has *mmrss* much higher than all the other  
 478 models. This is explained by the use of the Grythe et al. (2014) source function with size  
 479 bins up to  $20 \mu\text{m}$  radius. First, the other CMIP6 models only emit up to a maximum ra-  
 480 dius of  $\sim 10 \mu\text{m}$ , so CNRM-ESM adds an extra mass in the  $10 \mu\text{m}$ – $20 \mu\text{m}$  range. Second,

481 the Grythe et al. (2014) source function has a coarse emission mode with a mean radius  
 482 of 30  $\mu\text{m}$ , inducing large emissions of coarse particles which strongly contribute to mass.  
 483 Figure 6a shows that for a maximum radius of 20  $\mu\text{m}$ , this source function yields a mass  
 484 flux one order of magnitude greater than any other model for a given wind speed of 10  $\text{m s}^{-1}$   
 485 and 5°C SST, which is the difference observed in Figure 4.

486 Figure 6a also shows that for a given choice of aerosol size bins (assuming a sectional  
 487 approach with mean radii 0.05-0.5-1- $R_{max}$   $\mu\text{m}$  and varying  $R_{max}$ ), selecting a source  
 488 function over another can change the flux by up to one order of magnitude (e.g. grey bar  
 489 for JA11 versus grey bar for GR14). Furthermore, the source functions do not have the  
 490 same sensitivity to the choice of the larger aerosol size. Some source functions are very  
 491 sensitive to the radius of the coarser section, which leads to large changes in the mass  
 492 flux (SM98, MA06 and GR14) with larger mass emissions for bigger particle bins. But  
 493 for the others, the number flux for larger particles decreases fast which causes the mass  
 494 flux to increase less as radii increase. For the SSAer emissions, although it is critical for  
 495 the wind speed (and SST when used) to be accurately represented, the diversity between  
 496 models is driven primarily by the choice of the source function formulation and aerosol  
 497 size bins rather than by meteorological differences (see Figure 6a and Figure 6b). When  
 498 changing wind speeds by  $\pm 1 \text{ m s}^{-1}$  (which is the spread found in CMIP6 models), the  
 499 impact on the mass emission flux is generally smaller than a change in the coarse mode  
 500 aerosol size bins. Figure 6b also shows the influence of accounting for SST in the source  
 501 function (blue and green stars). In general, changing the SST by  $\pm 5^\circ\text{C}$  leads to a sim-  
 502 ilar to smaller change in the mass emission flux than varying the wind speed by  $\pm 1 \text{ m s}^{-1}$ .  
 503 Since the spread in SST in CMIP6 models is less than 5°C, we therefore conclude that  
 504 the emission flux dependence on SST is not an important contributor to the CMIP6 model  
 505 diversity.

506 The fine aerosol size bins (taken here as 300 nm and smaller aerosol diameter) in-  
 507 fluence the number of SSAer potentially acting as CCN. BCC-ESM barely produces any  
 508 SSAer below 300 nm since the smaller aerosol bin considered has a minimum diameter  
 509 of 200 nm. For the other source functions, we compute the number emission flux con-  
 510 sidering the following SSAer diameter bins: [30-40-50-60-70-80-90-100-200-300] nm. In  
 511 this range of diameters, the total number flux of SSAer varies by a factor of 8, except for  
 512 the MO86 function which yields a number flux 2 orders of magnitude larger in this size  
 513 range. Therefore, for models including the interactions of aerosols with radiation and clouds,  
 514 the choice of source function can strongly influence the associated radiative impacts, as  
 515 illustrated in Prank et al. (2022).

516 In summary, the large variety in the magnitude of simulated SSAer concentrations  
 517 at the poles is driven primarily by the choice of aerosol emission sizes and the source func-  
 518 tion, and secondly by the meteorological drivers of emissions (open ocean fraction, wind  
 519 speed, mean planetary boundary layer height). The atmospheric processes (deposition,  
 520 transport, ageing) and thereby the residence time of SSAer drives the differences in spa-  
 521 tial distribution and concentrations over the ocean and land. The variety in seasonal-  
 522 ity is primarily driven by sea ice and meteorology, with diverse sea ice concentration and  
 523 wind speed annual cycles modulating emissions, but also heterogeneity in the represen-  
 524 tation of the planetary boundary layer and deposition which influence concentrations ir-  
 525 respective of the emission flux. The choice of aerosol sizes and source function formu-  
 526 lation also affects the number of SSAer that could act as CCN.

## 527 3.2 Evaluation using observations

### 528 3.2.1 Comparison with ground based stations

529 Given the previously identified diversity in *mvrss* in the investigated CMIP6 mod-  
 530 els, a comparison with the observed sodium aerosol concentration from ground-based sta-  
 531 tions is conducted to evaluate individual model and ensemble performance (Figure 7, Fig-

532 ure 8 and Figure A2). Figure 7 summarizes the comparison between the annual cycle  
 533 of sodium near-surface concentration in the CMIP6 models and the measurements for  
 534 the 14 stations. The NMB and correlation of the annual cycle of individual models as  
 535 well as the ensemble mean are computed. Reanalysis data from MERRA2 and CAMS  
 536 are also included. The data from observations and models are averaged over the longest  
 537 available period for each of them, i.e. 1951–2014 for CMIP6, 1980–2021 for MERRA2,  
 538 2003–2021 for CAMS, and as indicated in Figure 1 for the measurements.

### 539 *Arctic*

540 For the Arctic stations, Figure 7 shows that most CMIP6 models have mean con-  
 541 centrations around two to eight times larger than observations. Except for one station  
 542 where it is negative, the correlation between the modeled and observed annual cycles of  
 543 concentrations are positive, and mostly above 0.5, indicating a reasonable seasonality.  
 544 At the Irafoss and Summit stations, the correlation coefficient between the CMIP6 en-  
 545 semble mean annual cycle and the observations is high, at 0.85 and 0.84, respectively,  
 546 despite NMB of up to one order of magnitude in individual models. At the Zeppelin, Utqiagvik,  
 547 Pallas, Karasjok and Breckälén stations, NMB and correlations are between 91% and  
 548 435%, and 0.61 and 0.81, respectively. Unlike the two previous ones, some models at these  
 549 four stations are not significantly correlated with the observations at the 95% level. Alert  
 550 and Villum stations are the only two locations where the NMB is relatively small, and  
 551 negative (around -20%). However, due to the low correlation (-0.45 at Alert, 0.44 at Vil-  
 552 lum), this relatively low NMB is not a sign of good performance, as discussed later.

553 In order to understand if the variation by season for SSAer is correctly represented  
 554 we apply a bias correction on CMIP6 model output (Figure 8). For each model, the an-  
 555 nual cycle is adjusted by the factor  $\bar{j}\text{OBS}_i/\bar{j}\text{MODEL}_i$ , which is the annual mean observed  
 556 sodium concentration divided by the annual mean in the model for each station. Using  
 557 the bias corrected data (Figure 8) for the Arctic stations Alert and Villum, CMIP6 mod-  
 558 els have very diverse annual cycles (the median correlation across models is not signif-  
 559 icant at the 90% level). The ensemble mean has no significant correlation with the cor-  
 560 responding observations at the 95% level (boundaries of the confidence interval have op-  
 561 posite signs). Also, the yearly maximum in Aug–Sep in the models contrasts with ob-  
 562 servations which are at their minimum during that period. For such high-latitude sta-  
 563 tions, where the Arctic Ocean is covered with sea ice throughout the year and the pro-  
 564 duction of sea spray does not occur, it is thought that the observed wintertime SSAer max-  
 565 imum originates from blowing snow on sea ice emissions (Yang et al., 2008; J. Huang &  
 566 Jaeglé, 2017; Yang et al., 2019) or from sea spray originating from leads (Held et al., 2011;  
 567 Kirpes et al., 2019). In CMIP6 models, these sources are not included in the param-  
 568 eterizations, which may explain the lack of correlation with observations at Alert and Vil-  
 569 lum and the negative NMB in wintertime. However, some models (UKESM and HadGEM)  
 570 seem to have the right seasonal cycle at Alert, without including a sea ice source of SSAer.  
 571 Additional analyses show that the emissions surrounding the location have a minimum  
 572 in winter, but the annual cycle of planetary boundary layer height varies more with sea-  
 573 son in UKESM and HadGEM compared to the other models, with higher values in sum-  
 574 mer and shallower heights in winter (see Figure A3). This explains the shape of the an-  
 575 nual cycle despite the absence of winter local sources in the models. Since winter sources  
 576 such as blowing snow are observed in measurements (Frey et al., 2020), these two mod-  
 577 els likely have the right annual cycle for the wrong reasons. Except at Utqiagvik where  
 578 the Dec–Jan high concentrations are missed by the models, the seasonality is reasonably  
 579 well captured by the ensemble mean at the other locations.

### 580 *Antarctic*

581 For Antarctic stations, the magnitudes of the NMB are similar to those of the Arc-  
 582 tic sites, except at Dumont d’Urville and Neumayer where several models have a rela-

583 tive NMB below 100% (Figure 7). The diversity between models is large as well, with  
 584 no significant across-model correlation at the 90% level for any station, and a strictly  
 585 positive correlation at the 95% level of the ensemble mean with observations only at Du-  
 586 mont d’Urville and Palmer stations (Figure 8). At Concordia station, two models ex-  
 587 hibit an Arctic-like cycle with maximum concentrations in Dec–Feb (MRI-ESM and MIROC-  
 588 ES2L), while the others produce an annual cycle with maximum concentrations in Jun–  
 589 Aug. In both groups, the clear maximum recorded by measurements in November is missed.

590 The models are relatively good at the coastal site of Dumont d’Urville, with a 0.64  
 591 correlation and a bias corrected annual cycle mostly within one standard deviation of  
 592 the observations (Figure 8). In contrast, at Concordia station which is 1200 km further  
 593 inland from Dumont d’Urville (Figure 1), the correlation with observations is not sig-  
 594 nificant at the 95% level and not one individual model is within one standard deviation  
 595 of the measurements. This difference in performance might be indicative of inadequate  
 596 removal processes over land. In particular, climate models at a resolution lower than 1°  
 597 tend to underestimate precipitation over Antarctica (Tang et al., 2018), which would re-  
 598 sult in too low wet deposition along transport, and therefore too high concentrations over  
 599 the continent, despite reasonable concentrations at the coast. In addition, the orogra-  
 600 phy of this region might not be well reproduced in climate models, which could lead to  
 601 inadequate dynamics and thus explain the shortcomings in CMIP6 in terms of the an-  
 602 nual cycle of SSaer.

603 At Halley station, the comparison is partially hindered by the relatively short length  
 604 of the observation records, which only cover 3 years and comprise a large variability, but  
 605 the CMIP6 bias-corrected values are mostly within one standard deviation of the obser-  
 606 vations for this station (Figure 8). At Neumayer station, the shape of the annual cycle  
 607 in the models is reasonable but is shifted two months too early compared to measure-  
 608 ments. At Dumont d’Urville, all models adequately produce a maximum in Dec–Feb, al-  
 609 though generally too high compared to observations and possibly one month late, which  
 610 leads to a distorted seasonal cycle. A similar comparison can be made for Palmer sta-  
 611 tion, although with a maximum delayed by two months compared to Dumont d’Urville.  
 612 These two latter stations are the lower latitude ones (north of 70°S) where the sea ice  
 613 maximum extent in winter is lower according to Figure 1. Like for the Arctic, the ab-  
 614 sence of a sea ice related SSaer source in the models (blowing snow, leads) degrades their  
 615 performance during winter.

### 616 *Reanalyses*

617 Two reanalysis data sets are also included in this analysis (Figure 7) and compared  
 618 to observations. MERRA2 is known to have a positive bias on SSaer mass concentra-  
 619 tion of around one order of magnitude even at lower latitudes (Kramer et al., 2020), which  
 620 was partly attributed to a distortion of the size distribution of SSaer, with too few small  
 621 particles and too many large ones (Bian et al., 2019). This is consistent with Figure 7  
 622 where MERRA2 is found to systematically overestimate concentrations with a larger pos-  
 623 itive NMB than the CMIP6 ensemble mean, for both poles, between 163% and 2,532%.  
 624 CAMS has a generally better performance than MERRA2, both in terms of correlation  
 625 and NMB, the latter being limited to 730% at most. Generally speaking, CAMS is less  
 626 biased than the CMIP6 ensemble, but has a lower correlation when it comes to repro-  
 627 ducing the observed annual cycle. These two comparisons show that despite being com-  
 628 monly used as validation data sets, reanalyses have difficulties in reproducing observed  
 629 SSaer concentrations at the poles, and have a generally poorer performance than the CMIP6  
 630 ensemble. However, since SSaer concentrations are not assimilated in these reanalyses,  
 631 and AOD is assimilated only as total AOD, a better performance than CMIP6 was not  
 632 expected.

633

### 3.2.2 Comparison of modeled SSAer AOD with MODIS AODss

634

635

636

637

638

639

640

641

642

643

644

645

646

AOD is often used to evaluate aerosols in climate models, since it is closely related to the full aerosol burden throughout the atmospheric column, including the impact of water uptake on aerosols. It is also more closely related to direct aerosol-radiation climate forcing than surface observations, and is less sensitive to errors in vertical aerosol distributions. SSAer AOD at 550 nm is provided for a subset of CMIP6 models including BCC-ESM, EC-Earth, IPSL-CM6, MPI-ESM, MRI-ESM, NorESM, and compared here to AODss at 550 nm extracted from MODIS Dark Target/Deep Blue satellite data (Figure 9). The monthly MODIS data are processed as described in Section 2.2.2 to approximate the contribution of SSAer to total AOD, noting that AOD is not available for cloud covered regions and ice/snow covered surfaces. MODIS data is also scarce during the polar night due to the absence of visible light. MODIS Terra and MODIS Aqua AODss are shown separately due to the differences between these two monthly AOD products (Sogacheva et al., 2020).

647

648

649

650

651

652

653

654

655

656

657

658

659

660

661

662

Figure 9 shows the magnitudes and spatial patterns of SSAer AOD in CMIP6 and AODss in MODIS, for the Arctic and the Southern Ocean. In the northern Atlantic, the CMIP6 ensemble median is around 0.02 (0.04, respectively) higher than MODIS Terra (Aqua, respectively). Spurious high AODss values in satellite data over the high Arctic (brown pixels in Figure 9 middle with AODss up to 1 on average) could be artifacts related to the scarcity of valid records available in the region (due to possible cloud contamination or poor snow/sea ice screening) making the comparison more difficult. For the Antarctic, values south of 60°S are comparable between CMIP6 SSAer AOD and MODIS AODss, below 0.02 in coastal regions with a positive northward gradient up to around 0.08 at 60°S. However, in the area between 50°S and 60°S, the band of maximum SSAer AOD in CMIP6 is not observed in the AODss MODIS data (Terra or Aqua), except for sporadic hot spots. For this area, the spatial distribution in MODIS is less homogeneous and has a lower AODss on average compared to CMIP6. Given the semi-permanent presence of clouds at these latitudes, around 90% annually (Lachlan-Cope, 2010), a sampling bias in the MODIS data cannot be excluded to account for this discrepancy, which does not invalidate the high values in CMIP6.

663

664

665

666

667

668

669

670

671

672

673

674

675

676

677

678

679

680

681

682

683

684

The spatially averaged SSAer AOD and AODss show reasonable agreement between CMIP6 and MODIS in terms of the annual cycle (Figure 9 right). For the Arctic, MODIS features a late winter (Feb–Mar) maximum in AODss that is not represented in the models, whereas most models have a maximum SSAer AOD in early winter (Dec–Jan) that is not found in MODIS and up to 0.1 higher than the MODIS values. However, for those winter months (Nov–Feb), the MODIS data are more sparse than in summer (Jun–Sep), which could result in another sampling bias (Figure 9 right - grey bars). Since cloud cover is lower in winter compared to summer (Eastman & Warren, 2010), and should therefore impede AOD retrieval less often, sea ice cover can explain the lack of records, in combination with the polar night. Sea ice is at its maximum extent and is too bright a surface for MODIS instruments to accurately separate the contribution to back-scattering from the ground and from aerosols (Mei et al., 2013), leading to fewer valid records in winter than in summer. On the other hand, the MODIS-derived annual cycle of AODss is quite similar to the cycle of total aerosol mass and surface area observed in Tunved et al. (2013), which could indicate limitations in our AODss extraction approach. Similarly, the scarcity of MODIS data in the Antarctic for Mar–Sep prevents such a comparison. Furthermore, the observed decrease in AODss in Apr–May could be due to a sampling bias, since MODIS records are less numerous south of 60°S compared to other months (Figure 9 - grey bars). For the austral summer months (Nov–Feb), when the comparison is less uncertain due to a larger number of available records, all the models are within one standard deviation of both MODIS Terra and Aqua values and closer to the Aqua mean. This is true for all the models in the Arctic, and most of them in the Antarctic.



685 tic. The shape of the monthly variations is reasonably well reproduced in both cases, except in winter.  
686

687 The CMIP6 ensemble is closer to MODIS Terra when it comes to climatological  
688 maps, but closer to MODIS Aqua for the summer months, when the comparison is more  
689 robust thanks to a larger number of MODIS records. The offset of around 0.02 obtained  
690 here between MODIS Aqua and MODIS Terra in our AODss product is well known and  
691 described in the literature, in which MODIS Aqua is considered to be more accurate than  
692 MODIS Terra (Sogacheva et al., 2020). Therefore, the better agreement of CMIP6 mod-  
693 els with MODIS Aqua in summer is an indication that the SSAer AOD is reasonably cap-  
694 tured in the CMIP6 models, although the model variability is large for the winter months.

695 Despite the fairly large discrepancies in *mmrss* revealed in Section 3.2.1, the SSAer  
696 AOD at 550 nm shows better performance in the CMIP6 models compared to the satel-  
697 lite data. This indicates that the direct radiative effect of SSAer is likely well reproduced  
698 for the poles as well. This also suggests, given the bias on surface mass concentrations,  
699 that (i) the size distribution of SSAer might not be adequate, possibly steered toward too  
700 coarse particles, or (ii) that the vertical distribution of SSAer is biased and accumulates  
701 too much mass at the surface. However, the good performance in SSAer AOD is not nec-  
702 essarily a sign of adequate fine mode number concentrations. Some models are known  
703 to have hygroscopic growth factors that are too high (Burgos et al., 2020), which can in-  
704 crease SSAer AOD despite incorrect (too low) quantities of fine fraction mode particles.  
705 Although this is not analyzed further in this work, compensating effects between num-  
706 ber, size and hygroscopicity of SSAer needs further investigation in the future.

### 707 **3.3 Implications for our understanding of polar climate**

708 In this section we address the implications of the diverse representation of SSAer  
709 in CMIP6 for our understanding of present and future climate. In what follows, we first  
710 evaluate the sensitivity of the polar climate to SSAer based on the CMIP6 *piClim-2xss*  
711 experiment. Then, historical and future trends of SSAer emissions and *mmrss* are inves-  
712 tigated under scenarios SSP126 and SSP585 to assess the uncertainty borne by climate  
713 projections owing to SSAer.

#### 714 **3.3.1 Radiative impact of SSAer**

715 The pre-industrial climate experiments from the AerChemMIP activity provide a  
716 control (*piClim-control*) and a doubled SSAer emission (*piClim-2xss*) experiment, for a  
717 30 year period under 1850 climate conditions. Three CMIP6 models provide the top-of-  
718 the-atmosphere net downward radiative flux (*rtmt*) for these experiments and are used  
719 in this section. The change in *rtmt* between the *2xss* and *control* experiments is used  
720 here to evaluate the radiative impact of SSAer. The entire 30 year period is considered.  
721 For the three models considered, this includes the aerosol-radiation interaction and the  
722 aerosol-cloud interaction, although they cannot be disentangled, since *rtmt* provides to-  
723 tal radiation only (short-wave + long-wave). The *piClim* simulations are fixed-sst, so that  
724 *rtmt* includes the effect of rapid atmospheric adjustments, but not the effect of climate  
725 feedbacks from long-term surface temperature change. In this respect, the *rtmt* change  
726 is comparable to an effective radiative forcing.

727 One important factor for the direct and indirect radiative effects of SSAer is their  
728 vertical distribution. We show the diversity in the vertical distribution of both SSAer and  
729 clouds in Figure A4 for ocean/ice covered regions north/south of 60°N/S. There is a large  
730 diversity between modeled profiles, of more than two orders of magnitude above 5,000 m  
731 altitude for SSAer, and a factor of around 10 in clouds throughout the column. This sug-  
732 gests that the radiative impact of SSAer can also be assumed to be very diverse and un-  
733 certain.

734 Figure 10 shows the average change in  $rtmt$  between the doubled SSAer emissions  
 735 and the control experiment, for summer months and winter months in the Arctic and  
 736 Antarctic. In summer, when sea ice extent is at its minimum in the Antarctic, the ra-  
 737 diative impact of SSAer is mostly negative (cooling effect) in the three models over the  
 738 ocean, with up to  $-10 \text{ W m}^{-2}$  in NorESM and  $-5 \text{ W m}^{-2}$  in IPSL-CM6 and UKESM (Fig-  
 739 ure 10). This important change is probably partly related to the aerosol-cloud interac-  
 740 tion and its albedo effect over darker surfaces (open ocean), as found in Struthers et al.  
 741 (2011). The aerosol direct effect also likely contributes to this change, especially in NorESM  
 742 where the change in AOD is large over the Southern Ocean, with more than  $+0.25$  on  
 743 average (Figure A5). Such an important change is not found in the other models for the  
 744 Southern Ocean (less than  $+0.1$ ), explaining why the cooling effect is larger in NorESM  
 745 in summer in the Antarctic than in IPSL-CM6 and UKESM.

746 Over the Antarctic continent in summer, for most areas the radiative impact can-  
 747 not be significantly distinguished from zero at the 90% level according to a Wilcoxon test,  
 748 but regionally averaged south of  $60^\circ\text{S}$ , a negative radiative impact significant at the 95%  
 749 level is found, comprised between  $-0.34 \pm 0.02 \text{ W m}^{-2}$  and  $-1.01 \pm 0.07 \text{ W m}^{-2}$  (Table 2).  
 750 In winter, when sea ice extent is larger and there are fewer areas prone to sea spray pro-  
 751 duction in the region, the radiative impact is slightly positive in West Antarctica but mostly  
 752 not significantly different from zero at the 90% level in the region when considering all  
 753 three models (Figure 10 and Table 2).

754 NorESM and UKESM indicate a cooling effect in the high Arctic in winter, with  
 755 a regionally significant negative radiative impact at the 95% level (Table 2). IPSL-CM6  
 756 suggests a small heating effect in northeastern Canada and a slight heating in the high  
 757 Arctic for Dec–Feb, although the regional average is smaller than the cooling obtained  
 758 in the other models. In summer, the changes are stronger and more heterogeneous, with  
 759 regions of large cooling next to regions of large heating, although generally not signif-  
 760 icant at the 90% level (Figure 10), resulting in a regionally weak cooling effect overall  
 761 in all the models (Table 2). The weak change in AOD in summer can partially explain  
 762 this moderate radiative effect (Figure A5).

763 The effects of doubling SSAer can be further described in terms of changes in air  
 764 surface temperature ( $tas$  variable in CMIP6), as shown in Figure A6. NorESM predicts  
 765 a warming in the winter both in the Arctic and Antarctic ( $+0.20^\circ\text{C}$  and  $+0.17^\circ\text{C}$ , re-  
 766 spectively), while the response in the other models is either a slight cooling or warming,  
 767 but one order of magnitude smaller. In the summer, models agree on a cooling effect in  
 768 the Arctic ( $-0.013^\circ\text{C}$  to  $-0.078^\circ\text{C}$ ), while the sign of the change is uncertain in the Antarc-  
 769 tic (the average of the three models shows a zero net change). In the winter, these changes  
 770 in temperature are equally driven by oceanic and land regions, whereas in the summer  
 771 the temperature change is mainly found above land. This may be related to the more  
 772 homogeneous surface albedo in winter when sea ice extent is large and land is covered  
 773 in snow, whereas in summer the heat capacity of the open ocean contrasts with that of  
 774 the land. These changes in surface temperature are not directly connected to the changes  
 775 in top-of-the-atmosphere radiation found in Table 2, particularly in the Antarctic where  
 776 the large summer decrease in radiation in NorESM ( $-1.01 \text{ W m}^{-2}$ ) yields a surface warm-  
 777 ing of  $+0.065^\circ\text{C}$ . Cooling/heating effects over land/ocean which have different heat ca-  
 778 pacity and albedo may be at play in this case. The vertical distribution of the changes  
 779 in radiation may also play a role.

780 Figure A6 also shows the same change in surface temperature but in the *piClim-*  
 781 *2xdust* experiment, where dust emissions are doubled, instead of SSAer. In the Antarc-  
 782 tic, both species have similar impacts on surface air temperature (very limited in sum-  
 783 mer months, slight warming in winter months, on average). In the Arctic, dust have a  
 784 cooling effect in winter, of the same magnitude as the warming induced by SSAer, whereas  
 785 in summer, the cooling from SSAer is one order of magnitude larger than the cooling from  
 786 dust. The changes are also more widespread around zero in the case of SSAer, with wider

distributions than for dust, suggesting a greater sensitivity to SSAer than dust. Compared to SSAer, dust has limited local sources at the poles and mostly comes from long-range transport, which explains its smaller regional impact. However, this comparison speaks to the relevance of evaluating more closely SSAer and their climate impacts at the poles, which are comparatively less studied than for dust.

The implications of the previous analyses are not straightforward, since the *piClim* experiments consider pre-industrial atmospheric conditions, free of the current anthropogenic background. Although polar regions remain relatively pristine areas, they are affected by the transport of anthropogenic emissions from lower latitudes through warm air mass intrusions (Li & Barrie, 1993; Quinn et al., 2002; Dada et al., 2022). The non-linearity of aerosol-cloud interactions (Gryspeerd et al., 2019) requires an adequate aerosol background, including anthropogenic sources, to obtain reasonable estimates of the indirect effect of SSAer emissions and therefore its radiative impact. Furthermore, the radiative impact depends not only on the proper representation of the number and sizes of SSAer, but also on their hygroscopicity, particularly for the direct effect (Zieger et al., 2017), which are quite uncertain according to Section 3.1.

The relatively strong effect on radiation of doubled SSAer emissions puts Figures 2, 3 and 5 into perspective: the difference in SSAer emissions between two models can be up to a factor of 4, which according to Figure 10 should mean that the resulting radiative budget at the poles could differ by up to  $2 \text{ W m}^{-2}$  (depending on the season and the model). This suggests that the uncertainty on the polar radiative budget related to SSAer within CMIP6 models could have the same magnitude as the 20<sup>th</sup> century increase in global radiative forcing (Myhre et al., 2013). These numbers are in line with those from Struthers et al. (2011), where a 23% increase in SSAer AOD in the Arctic is estimated to result in a  $-0.2$  to  $-0.4 \text{ W m}^{-2}$  radiative impact.

### 3.3.2 Historical and future trends

As a result of polar amplification, the polar climate is changing even more dramatically than the global climate. Given the connection of sea spray emissions with sea ice and atmospheric dynamics (e.g. wind speed), significant trends can be anticipated in SSAer both in present day and future scenarios. These are investigated using ScenarioMIP experiments SSP126 and SSP585 (O'Neill et al., 2016). The analysis conducted hereafter is restricted to the six CMIP6 models that provide *mmr<sub>ss</sub>* in both scenarios, namely GISS, HadGEM, MIROC-ES2L, MRI-ESM, NorESM and UKESM. We note that observations do not have long enough time series to compute multidecadal trends for validation purposes.

In the historical period 1951–2014, the mass emission flux of SSAer in the polar regions generally increased and comparatively more homogeneously in the Southern Ocean than in the Arctic (Figure 11 top). In the latter region, emissions increased more strongly in the Barents Sea and Greenland Sea, at a rate of up to +6% per decade. In the high Arctic, this trend is lower, between +1.5% and +3% per decade, with no trend between  $-60^\circ\text{E}$  and  $-180^\circ\text{E}$ . In the Southern Ocean the increasing trend is more homogeneous, between +1.5 and +6% per decade in most of the area. For the Arctic and Antarctic, the historical trend is mainly driven by sea ice retreat, although a slight increase in wind speed is also found in the Antarctic (Figure A7). This Antarctic increase in SSAer is consistent with the findings of Korhonen et al. (2010). To some extent, the difference in trends of wind speed between the Arctic and Antarctic might be related to an asymmetry in the trends and dynamics of stratospheric ozone depletion (Turner et al., 2009).

Future scenarios in CMIP6 follow the Shared Socioeconomic Pathway (SSP) trajectories (O'Neill et al., 2016). Here, we consider the two extreme scenarios, SSP126 and SSP585. SSP126 represents the low end of the range of plausible future pathways, where radiative forcing reaches a level of approximately  $2.6 \text{ W m}^{-2}$  in 2100 compared to the pre-

838 industrial period. SSP585 is at the other end of the spectrum, with a radiative forcing  
 839 of approximately  $8.5 \text{ W m}^{-2}$  at the end of the century. In both of these scenarios, the  
 840 Arctic surface air temperature warms more than the global mean. The change in tem-  
 841 perature between 2000–2014 and 2085–2100 is different by a factor of around 2 between  
 842 the global and Arctic average ( $3.8^\circ\text{C}$  versus  $1.5^\circ\text{C}$  in SSP126 and  $10.8^\circ\text{C}$  versus  $5.1^\circ\text{C}$   
 843 in SSP585, respectively), and with a large uncertainty (model spread of  $7^\circ\text{C}$  in SSP126  
 844 and  $10^\circ\text{C}$  in SSP585). In contrast, the Antarctic has a lower warming than the global  
 845 mean in both scenarios (Table A1).

846 The spatially averaged time series of the yearly surface *mmrss* (Figure 11) show  
 847 different behaviors between the two poles over the historical period and in the two fu-  
 848 ture scenarios SSP126 and SSP585. In the Arctic, in scenario SSP585, each individual  
 849 model features an increasing trend resulting in the multiplication of surface *mmrss* by  
 850 a factor of 1.75 to 2.8 in 2099 compared to the 1951–1971 average (hereafter referred to  
 851 as baseline). In the ensemble mean, this increase is by a factor of 2.2. In the SSP126 sce-  
 852 nario, three models show a stabilization after 2050 and a slight decrease at the end of  
 853 the century. The two remaining models feature a stronger increase, lasting until the end  
 854 of the century and reaching levels comparable to those obtained in some models in SSP585.  
 855 The associated ensemble mean stabilizes at just under a 1.5 increase at mid-century com-  
 856 pared to the baseline. These trends mirror the trends in Arctic sea ice in the CMIP6 mod-  
 857 els analyzed in Notz and SIMIP Community (2020), showing decreasing sea ice cover un-  
 858 til 2050, followed by a stabilization in SSP126 and a continuous decrease until the end  
 859 of the century in SSP585. As a result, differences in trends in individual models might  
 860 come from differences in their underlying sea ice evolution. In the Antarctic, the SSP585  
 861 trajectory is similar to that in the Arctic, except for a smoother increase, by no more  
 862 than a factor of 2 in the more extreme model. Contrary to the Arctic, the increasing trend  
 863 in *mmrss* starts in the 1980s, and the SSP126 and SSP585 trajectories start separating  
 864 only around the year 2030, after which *mmrss* reaches a plateau in SSP126 until the end  
 865 of the century. For both poles, NorESM, which is the only model in this analysis that  
 866 includes an SST dependence in its sea spray source function, and which is not based on  
 867 a whitecap approach, shows the smallest increase in concentration at the end of the cen-  
 868 tury, in SSP126 and SSP585. This is consistent with Figure 6 which showed that for in-  
 869 creased SST, the SSAer mass flux decreases in the SA15 source function. As a result, in  
 870 a warming climate, accounting for the increase in SST decreases the SSAer mass flux at  
 871 the poles compared to not accounting for it. Generally speaking, the trends in all the  
 872 models are marginally larger in winter than in summer. For comparison, mid-latitude  
 873 oceans do not show historical or future trends in *mmrss*.

874 In addition to following different trajectories, future trends in surface *mmrss* in the  
 875 Arctic and Antarctic also have a different spatial distribution, although in both cases a  
 876 slight negative trend is found over land in Greenland and the Antarctic continent (Fig-  
 877 ure A8). This negative trend over land can be explained by increasing precipitation, and  
 878 therefore decreased aerosol residence time, in SSP scenarios in the Arctic (McCrystall  
 879 et al., 2021) and over Antarctica (Tewari et al., 2022). All of the Arctic Ocean where sea  
 880 ice can currently be found features a strong decreasing trend in sea ice concentration (Fig-  
 881 ure A8), which explains the strong increasing trend in *mmrss* in scenario SSP585. In con-  
 882 trast, the trend in the Antarctic is mainly driven by increasing *mmrss* in the Belling-  
 883 shausen Sea, and marginally by localized spots in the Wedell Sea, which appear to be  
 884 sea ice driven (Figure A8).

885 A multiplication of SSAer mass emissions in the Arctic by 3 in SSP585 (as indicated  
 886 by the CMIP6 ensemble mean) could imply a regionally negative radiative impact of around  
 887  $-1 \text{ W m}^{-2}$  to  $-2 \text{ W m}^{-2}$  in winter at the end of the century based on Section 3.3.1 (see  
 888 Figure 10 and Table 2). In particular, UKESM that showed a high sensitivity to dou-  
 889 bled SSAer emissions (Table 2) is also the model with the largest future trends in sce-  
 890 nario SSP585. The limited emission trend in the Antarctic, including in SSP585, sug-

gests a smaller counteracting effect of SSAer on polar warming. Nevertheless, these changes in mass emissions do not necessarily translate into a similar change in number of SSAer, and the latter can have a large impact on the indirect effect of SSAer. No information on the change in number of aerosols is available in CMIP6 models to further investigate these future trends in radiative effect, making them quite uncertain.

## 4 Conclusions and Perspectives

This work evaluates the representation of SSAer in polar regions within CMIP6 including a comparison to surface station observations and satellite AOD. Implications for the radiative balance at the poles in the present-day and future climate are also investigated. We address the questions:

*How diverse are SSAer emissions/concentrations at the poles in CMIP6 models?*

The inter-model comparisons result in the same conclusions for the Arctic and Antarctic, with a large diversity (up to a factor of 5) in the magnitude of simulated surface mass concentration of SSAer. The spatial distribution is generally consistent between models although the amount of SSAer transported over land varies. Diversity is also important in emissions (factor 3), aerosol layer height (factor 7-8), lifetime (factor 9), optical depth (factor 4) and total deposition (factor 2-3), resulting in a generally uncertain SSAer budget at the poles in CMIP6.

*What are the drivers of this model diversity?* The model diversity in CMIP6 is driven by differences in the sea spray source function formulations and by the drivers of sea spray emission (wind speed, sea-ice cover). We also show large differences in residence time which affect the transport of SSAer and are responsible for model diversity over land. Other SSAer related variables such as AOD, aerosol layer height and deposition fluxes are also diversely represented. We show that even if the emissions were identical, the surface mixing ratio of SSAer would still be different due to different treatments of boundary layer dynamics, aerosol models (micro-physics, treatment internal/external mixing, hygroscopicity, size bins/modes), and deposition fluxes of the SSAer.

*How well do the CMIP6 models represent SSAer at the poles relative to surface observations and remote sensing?* The evaluation of the modeled surface concentrations of sodium mass against ground station observations shows there is a large positive bias of up to one order of magnitude in CMIP6 models. Once the mean bias is corrected, the seasonal variations of SSAer concentration are relatively well captured for lower-latitude stations. For high-latitude stations, there is a deformation of the annual cycle in models compared to observations. The absence of wintertime local sources of SSAer such as blowing snow over sea ice and emissions from open leads can be one reason for that. Possible biases in sea ice representation could also be responsible. Models that include a SST dependence in the SSAer source function are not less biased than ones that do not, because the effect of SST change is smaller than other sources of bias from source functions, meteorological drivers, and aerosol processing. Modeled SSAer AOD compares well with satellite data, potentially indicating that improvements could be made to the size distributions to overcome the discrepancy in concentrations, assuming that the hygroscopicity factor is adequately represented.

*What are the implications of model diversity and changes in SSAer emissions, for the present and future polar climate?* Pre-industrial and future climate CMIP6 experiments show that models agree that a doubling of SSAer emissions exerts a net negative radiative perturbation at the top of the atmosphere in summer in the Arctic and the Antarctic, with less agreement for the sign of the impact in winter. In terms of surface temperature, models agree on a cooling effect in summer in the Arctic but disagree on the sign of the change for winter and for the Antarctic. These impacts are generally heterogeneous in terms of their spatial distribution, but the large uncertainty in the present-day

941 emissions shown here means possibly an uncertainty of up to  $2 \text{ W m}^{-2}$  in the polar ra-  
942 diative budget. A multiplication of SSaer mass emissions in the Arctic by more than 2  
943 in SSP585 (as indicated by the CMIP6 ensemble mean) could imply a regionally neg-  
944 ative radiative impact around  $-1 \text{ W m}^{-2}$  in winter at the end of the century.

945 These conclusions highlight the need for additional research on the representation  
946 of SSaer at the poles. In particular, polar-specific source functions and size distribution  
947 could help improve the simulated concentrations according to our findings. Addition-  
948 ally, this work shows that aerosol-radiation and aerosol-cloud interactions of SSaer at  
949 the poles cannot be ignored in models and need to be activated and accurately repre-  
950 sented to obtain a reliable radiative budget, including to quantify anthropogenic aerosol  
951 radiative effects.

**Tables**

**Table 1.** CMIP6 models considered and their sea spray source function and emission drivers. MA06 is (Mahowald et al., 2006), MO86 is (Monahan et al., 1986), MA03 is (Mårtensson et al., 2003), JA11 is (Jaeglé et al., 2011), GR14 is (Grythe et al., 2014), GO03 is (Gong, 2003), SA15 is (Salter et al., 2015), and SM98 is (M. H. Smith & Harrison, 1998). For the limit radii of sea salt aerosols, values in *italic* indicate smallest/largest lognormal modes instead of cut-off sizes.

Model	Source function	Drivers	Limit radii ( $\mu\text{m}$ )	Data used								
				<i>mnrss</i>	<i>siconc</i>	<i>sfcWind</i>	<i>emiss</i>	<i>od550ss</i>	<i>bldep</i>	<i>dryss/wetss</i>	<i>piClim</i>	<i>SSP</i>
BCC-ESM	MA06	Wind	0.1-10			x		x				
CESM	MO86, MA03	Wind, SST	0.02-10			x			x	x		
CNRM-ESM	JA11, GR14	Wind, SST	0.03-20			x						
EC-Earth	GO03, SA15	Wind, SST	<i>0.09-0.794</i>			x	x	x	x			
GISS	MO86	Wind	0.1-4			x		x	x			x
HadGEM	GO03	Wind	0.05-5			x		x	x			x
IPSL-CM6A	MO86, SM98	Wind	<i>0.1-1.185</i>			x	x	x	x	x	x	
MIROC-ES2L	MO86	Wind	0.1-10			x		x	x			x
MPI-ESM	MO86, SM98	Wind	<i>0.5</i>			x	x	x	x			
MRI-ESM	MO86	Wind	<i>0.13-1.75</i>			x	x	x	x			x
NorESM	SA15	Wind, SST	<i>0.0475-0.75</i>			x	x	x	x	x	x	x
UKESM	GO03	Wind	0.05-5			x		x	x		x	x

**Full model names and CMIP6 references**

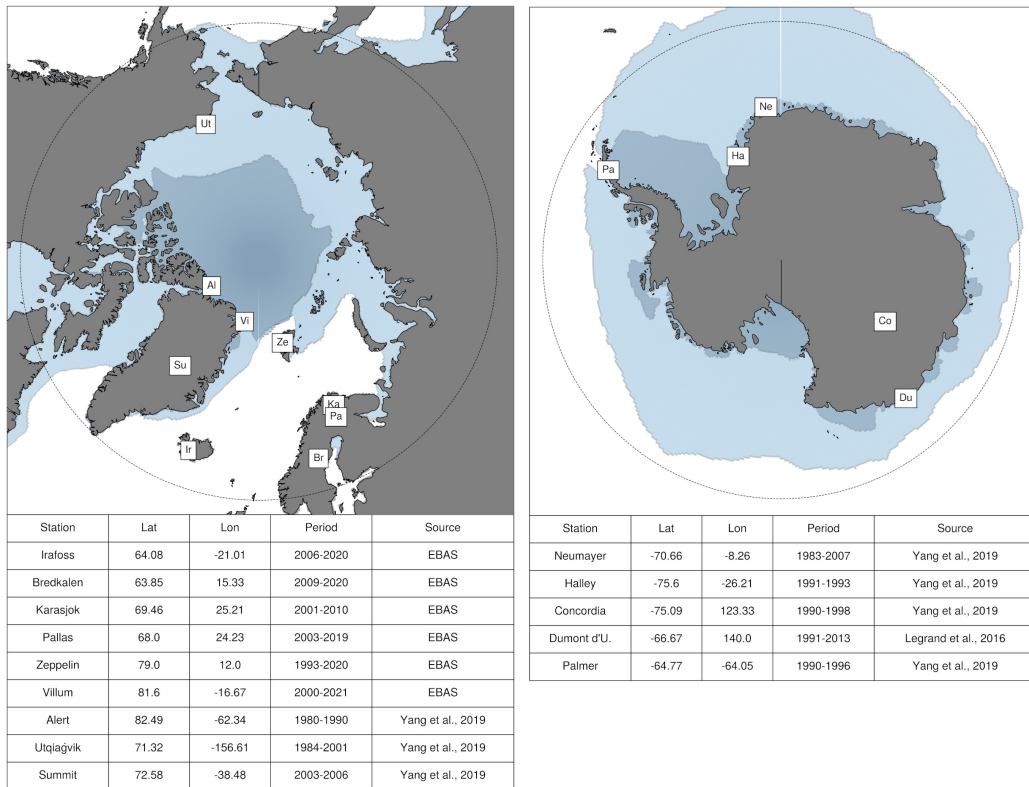
The Beijing Climate Center Earth System Model (Wu et al., 2020) – BCC-ESM1  
 The Community Earth System Model (Danabasoglu et al., 2020) – CESM2  
 The Centre National de Recherches Météorologiques Earth System Model (Séférian et al., 2019) – CNRM-ESM2-1  
 The European Community Earth System Model (Döscher et al., 2022) – EC-Earth3-AerChem  
 The NASA Goddard Institute for Space Studies Earth System Model (Miller et al., 2021) – GISS-E2-1-H  
 The Hadley Centre Global Environmental Model (Sellar et al., 2020) – HadGEM3-GC31-LL  
 The Institut Pierre Simon Laplace Climate Model (Boucher et al., 2020) – IPSL-CM6A-LR-INCA  
 The Model for Interdisciplinary Research on Climate Earth System for Long-term simulations (Hajima et al., 2020) – MIROC-ES2L  
 The Max Planck Institute Earth System Model (Gutjahr et al., 2019) – MPI-ESM-1-2-HAM  
 The Meteorological Research Institute Earth System Model (Yukimoto et al., 2019) – MRI-ESM2-0  
 The Norwegian Earth System Model (Seland et al., 2020) – NorESM2-LM  
 The UK Earth System Model (Sellar et al., 2020) – UKESM1-0-LL

**Table 2.** Regionally averaged mean change in top-of-the-atmosphere net downward radiation between the *piClim-2xss* and *piClim-control* scenario.  $\pm$  indicate 95% confidence intervals. Bold values indicate that the radiative impact is significant at the 95% level according to a Wilcoxon test. Arctic is all grid points north of 60°N and Antarctic is all grid points south of 60°S.

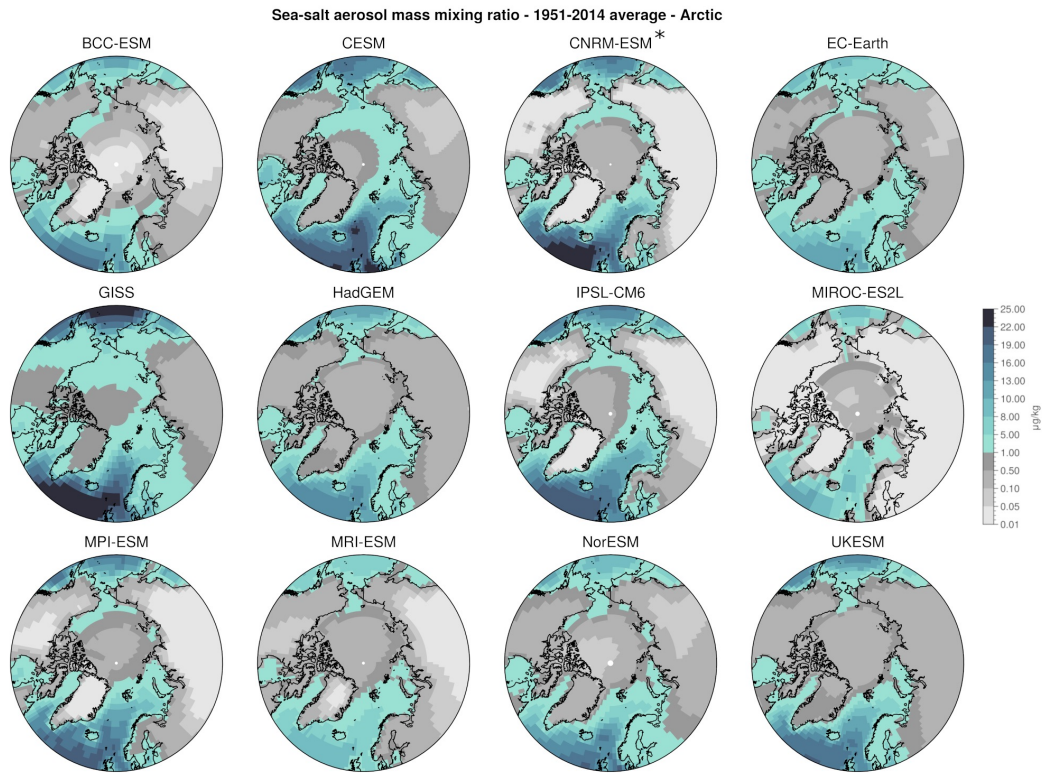
	Arctic		Antarctic	
	Dec–Feb	Jun–Aug	Jun–Aug	Dec–Feb
IPSL-CM6	<b>0.17±0.01</b>	<b>-0.48±0.03</b>	0.01±0.008	<b>-0.34±0.02</b>
NorESM	<b>-0.61±0.01</b>	<b>-0.29±0.04</b>	<b>-0.12±0.01</b>	<b>-1.01±0.07</b>
UKESM	<b>-0.33±0.01</b>	<b>-0.24±0.01</b>	<b>0.09±0.005</b>	<b>-0.37±0.02</b>



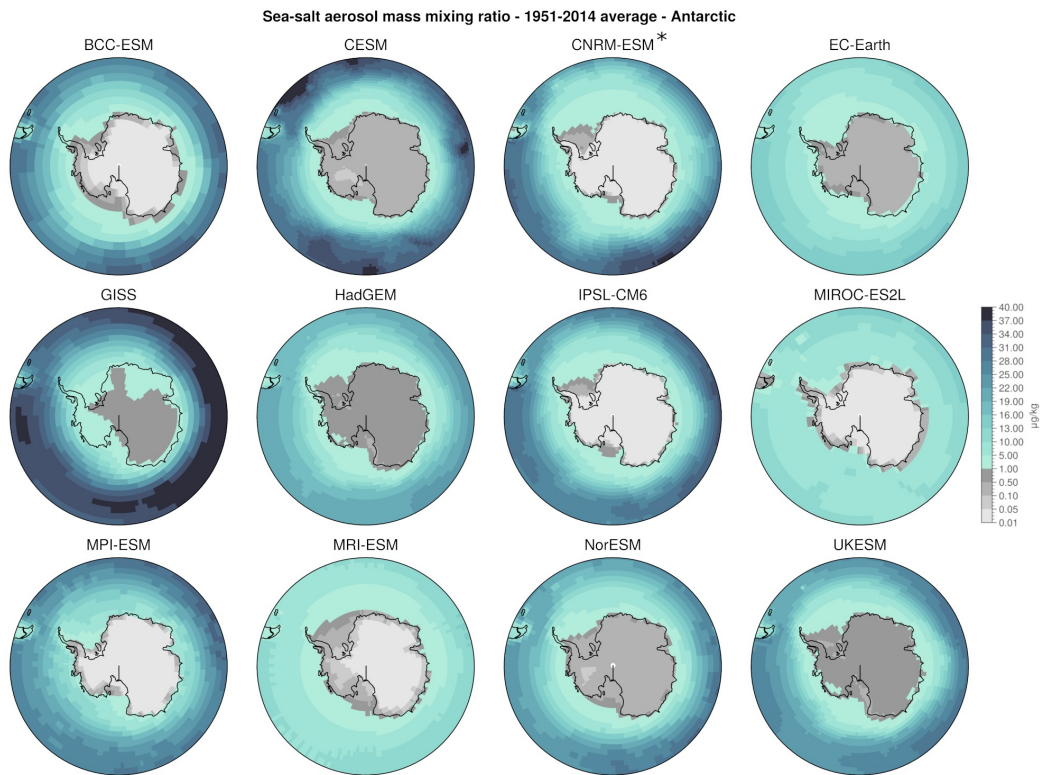
953 **Figures**



**Figure 1.** Arctic and Antarctic measurement stations providing sea salt surface mass concentration data. Blue colormaps indicate areas with a sea ice concentration above 50%. The lighter blue is for February in the Arctic, and August in the Antarctic. The darker blue is the opposite. The sea ice data are from ERA5. The black dashed line shows the 60° limit considered for regional aggregated analyses. Abbreviations in the maps are the first two letters of the corresponding station name.



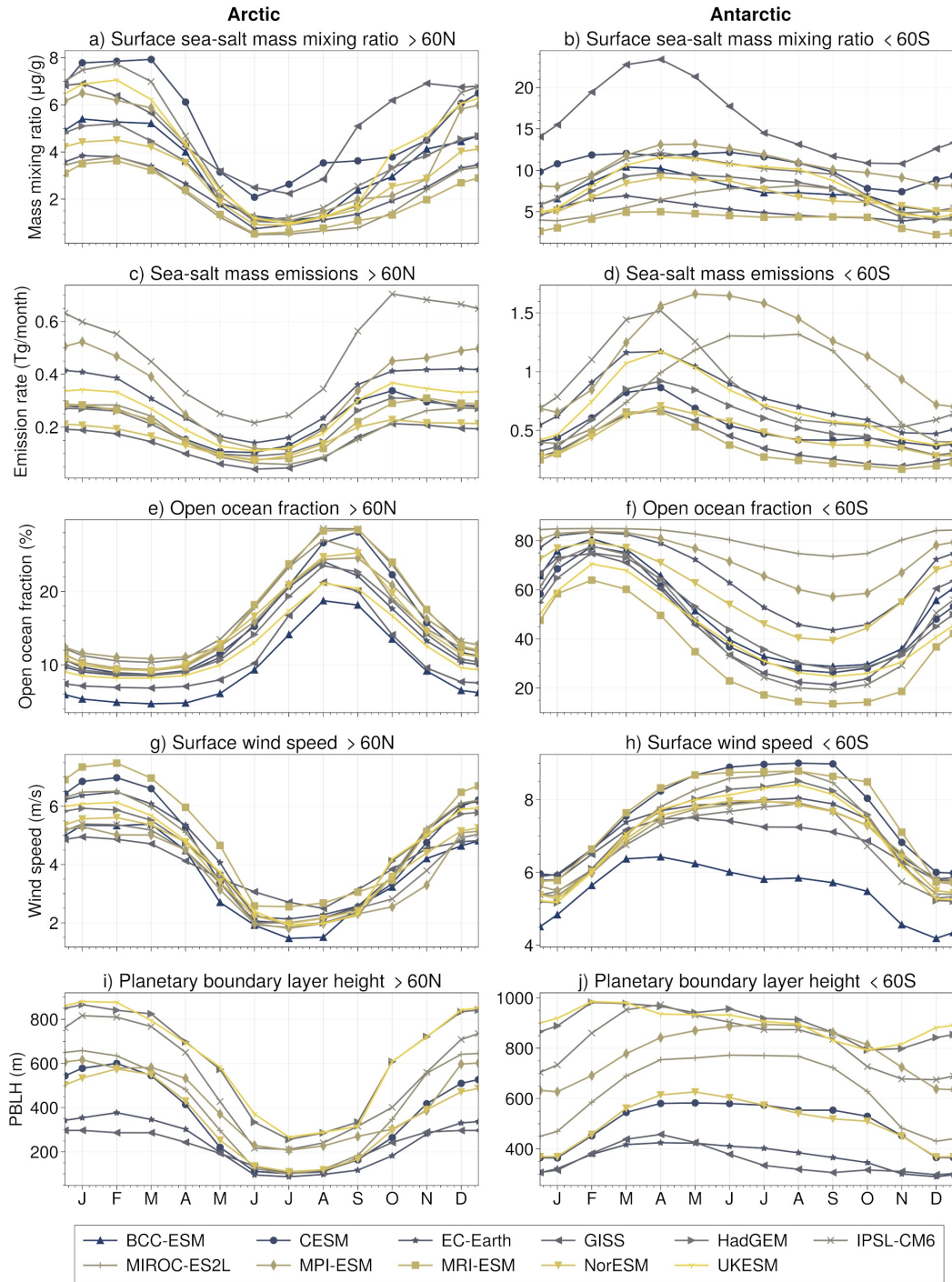
**Figure 2.** Sea salt aerosol mass mixing ratio in the lowest model level. Annual average for the period 1951–2014 in the CMIP6 historical scenario. Arctic map. NB: CNRM-ESM values are divided by 25 to fit in the colorbar.



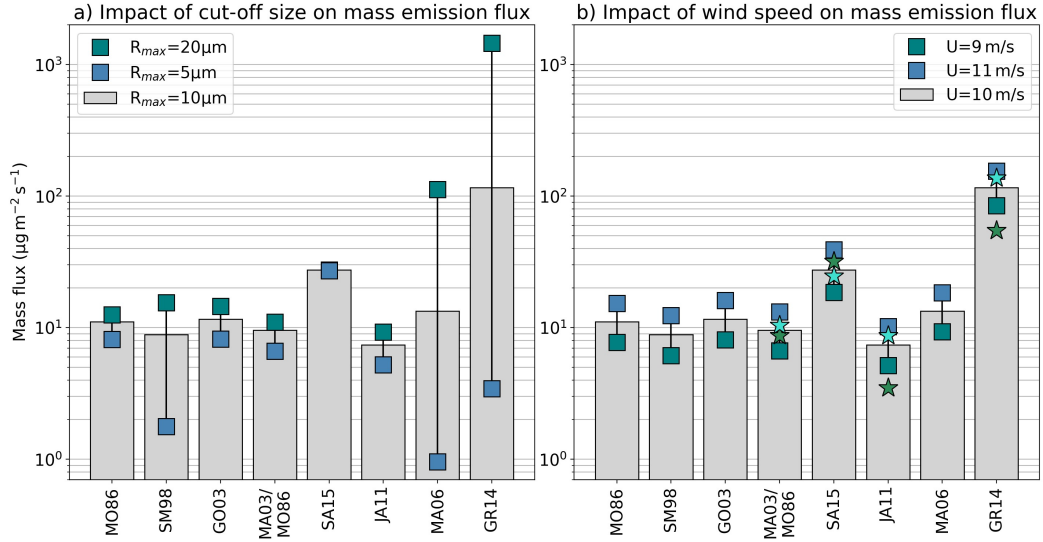
**Figure 3.** Same as Figure 2 but for the Antarctic.

	>60N						<60S						Global
BCC-ESM		11	207	4				43	224	13			
CESM	88	27	956		28	54	187	57	943		63	121	55
CNRM-ESM	3922	500	289	5			6973	1020	425	7			6
EC-Earth	120	14	515	6	99	30	272	35	655	17	220	59	14
GISS	53	31	299	90	12	54	135	109	314	201	31	132	29
HadGEM	82	15	581				201	42	667				18
IPSL-CM6	186	23	138	11	177	25	304	46	116	12	286	28	7
MIROC-ES2L	72	7	205		22	35	309	40	223		83	122	6
MPI-ESM	131	20	202	6	26	86	424	75	203	15	95	245	19
MRI-ESM	79	10	168	11	53	34	124	21	189	15	90	46	8
NorESM	64	14	479	15	26	39	161	44	566	29	58	83	34
UKESM	100	16	573				249	47	656				14
	Mass emissions (Tg/yr)	Mass mixing ratio ( $\times 10^{-6}$ g/g)	Aerosol layer height (m)	AOD ( $\times 1000$ )	Dry deposition (Tg/year)	Wet deposition (Tg/year)	Mass emissions (Tg/yr)	Mass mixing ratio ( $\times 10^{-6}$ g/g)	Aerosol layer height (m)	AOD ( $\times 1000$ )	Dry deposition (Tg/year)	Wet deposition (Tg/year)	Lifetime (hour)

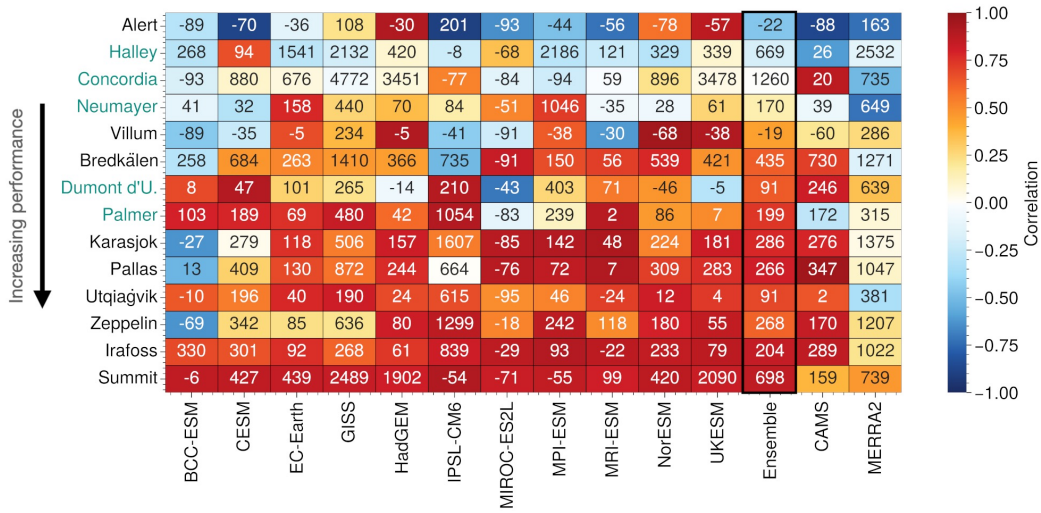
**Figure 4.** Model diversity in mass emissions, surface mass mixing ratio, aerosol layer height, AOD, dry and wet deposition, and lifetime of sea salt aerosol. Average for the period 1951–2014. The color scale highlights the highest values for each column. CNRM-ESM is excluded from this color scale for mass emission and *mmrss*. Empty cells indicate that values are not provided by the model. *mmrss* is multiplied by 10 and AOD is multiplied by 1000 for improved readability.



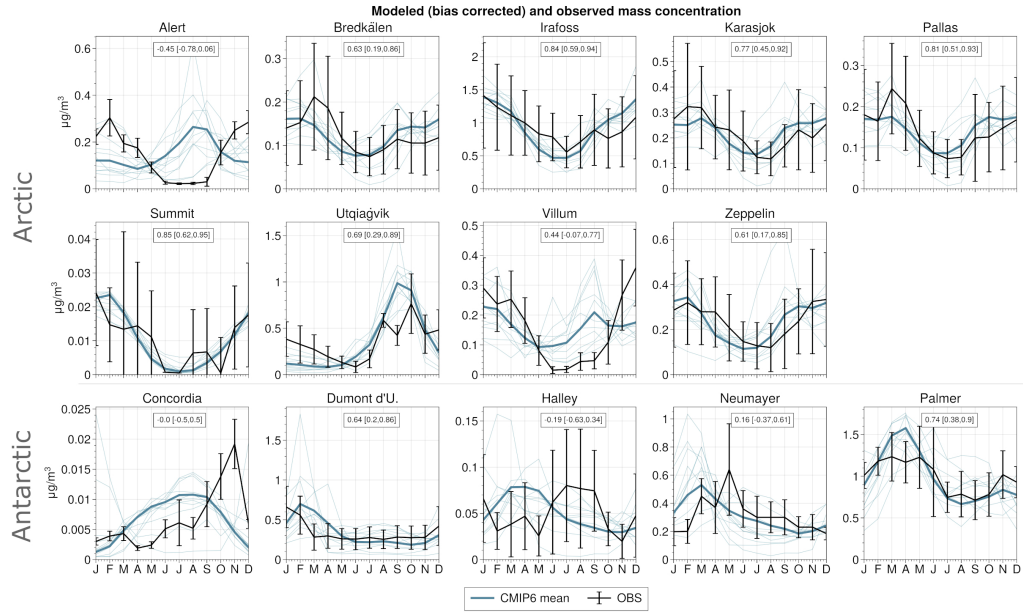
**Figure 5.** Annual cycles of sea salt aerosol mass mixing ratio at surface level (a,b), sea salt aerosol mass emission (c,d), fraction of open ocean (e,f), surface wind speed (g,h) and planetary boundary layer height (i,j) at latitudes above  $60^{\circ}\text{N}$  (left) and below  $60^{\circ}\text{S}$  (right) in CMIP6 models for the period 1951–2014. Lines show the monthly average over the period for each model. Emissions are summed to obtain the total emission flux over the considered region. Mixing ratio, wind speed and planetary boundary layer height are averaged for grid points over the ocean, with non-zero emissions and less than 90% sea ice cover. The open ocean fraction is computed as one minus the average of the sea ice concentration over the considered region. Panels (i,j) only include the 9 models providing the *bldep* variables (i.e. all except BCC-ESM, CNRM-ESM and MRI-ESM). Panels (c,d) do not include BCC-ESM as emission rates are not available for that model. CNRM-ESM is not included in this analysis.



**Figure 6.** Sea salt aerosol source functions used in CMIP6 models. a) effect on the mass emission flux of changing the aerosol cut-off radius, at  $10\text{ m s}^{-1}$  wind speed and  $5^\circ\text{C}$  SST. b) effect of changing wind speed on the mass emission flux for a cut-off radius at  $10\mu\text{m}$ . Green and blue stars indicate mass emission fluxes for  $0$  and  $10^\circ\text{C}$  SST, respectively, at  $10\text{ m s}^{-1}$  wind speed. In both panels, size bin limits are taken as  $0.05\text{-}0.5\text{-}1\text{-}R_{max}\mu\text{m}$ .

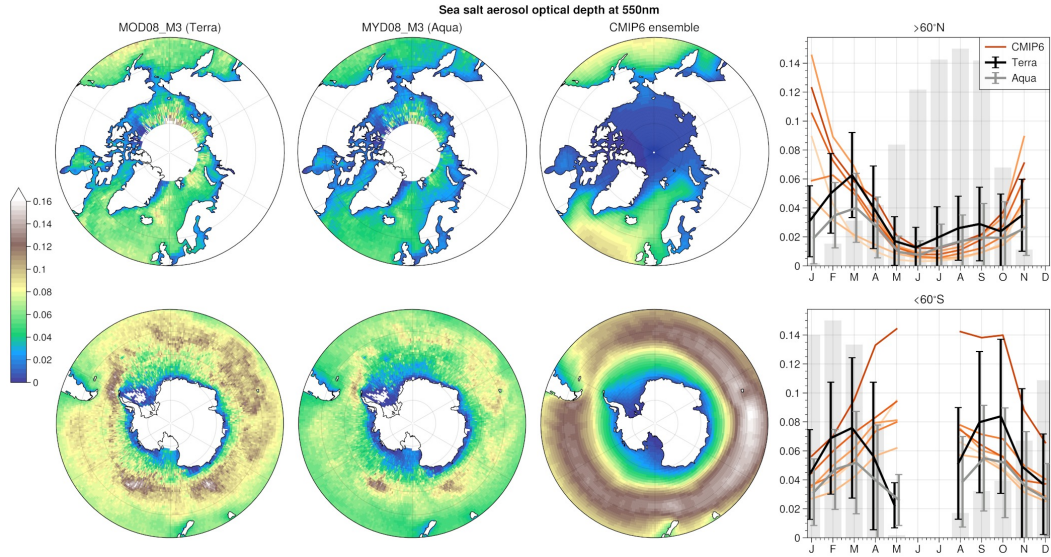


**Figure 7.** Normalized mean bias (numbers, in percent) and Pearson correlation coefficient (colormap) with respect to 9 stations in the Arctic (in black) and 5 stations in the Antarctic (in blue). CMIP6 individual models and ensemble mean are for the period 1951–2014, CAMS reanalysis is for 2003–2021 and MERRA2 is for 1980–2021. See Figures 8 and A2 for individual comparisons of time series.

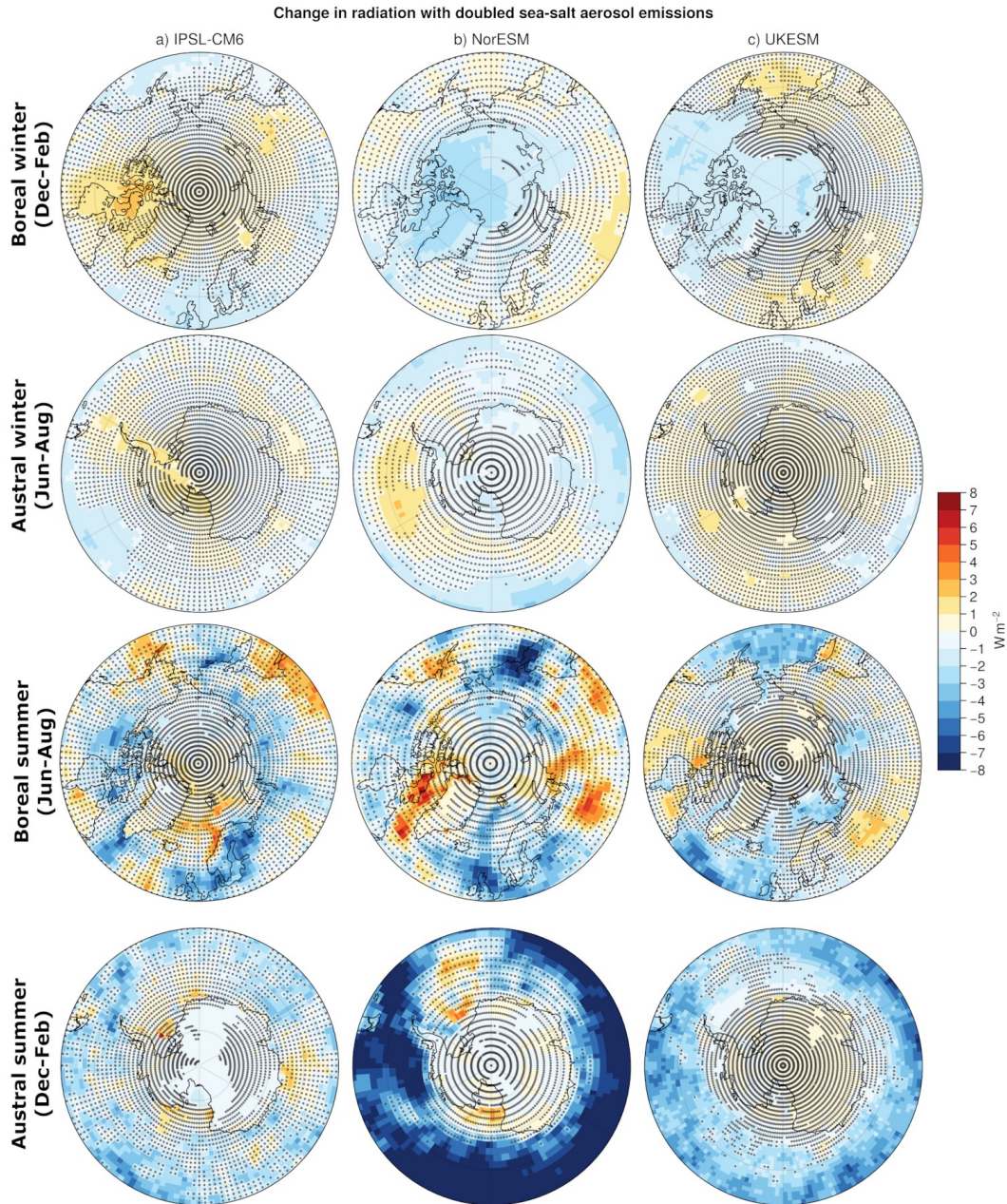


**Figure 8.** Annual cycle of sodium aerosol surface mass concentrations at 9 stations in the Arctic (top and middle) and 5 stations in the Antarctic (bottom). Observations are in black (caps show one standard deviation of monthly means), individual CMIP6 models (1951–2014) are in light blue, CMIP6 ensemble mean (solid thick line) is in blue. CMIP6 values are bias corrected by applying a factor  $\overline{OBS}_i / \overline{MODEL}_i$ . Boxes indicate the Pearson correlation coefficient between the annual cycle in CMIP6 ensemble mean and observations, with the 95% confidence interval between brackets.

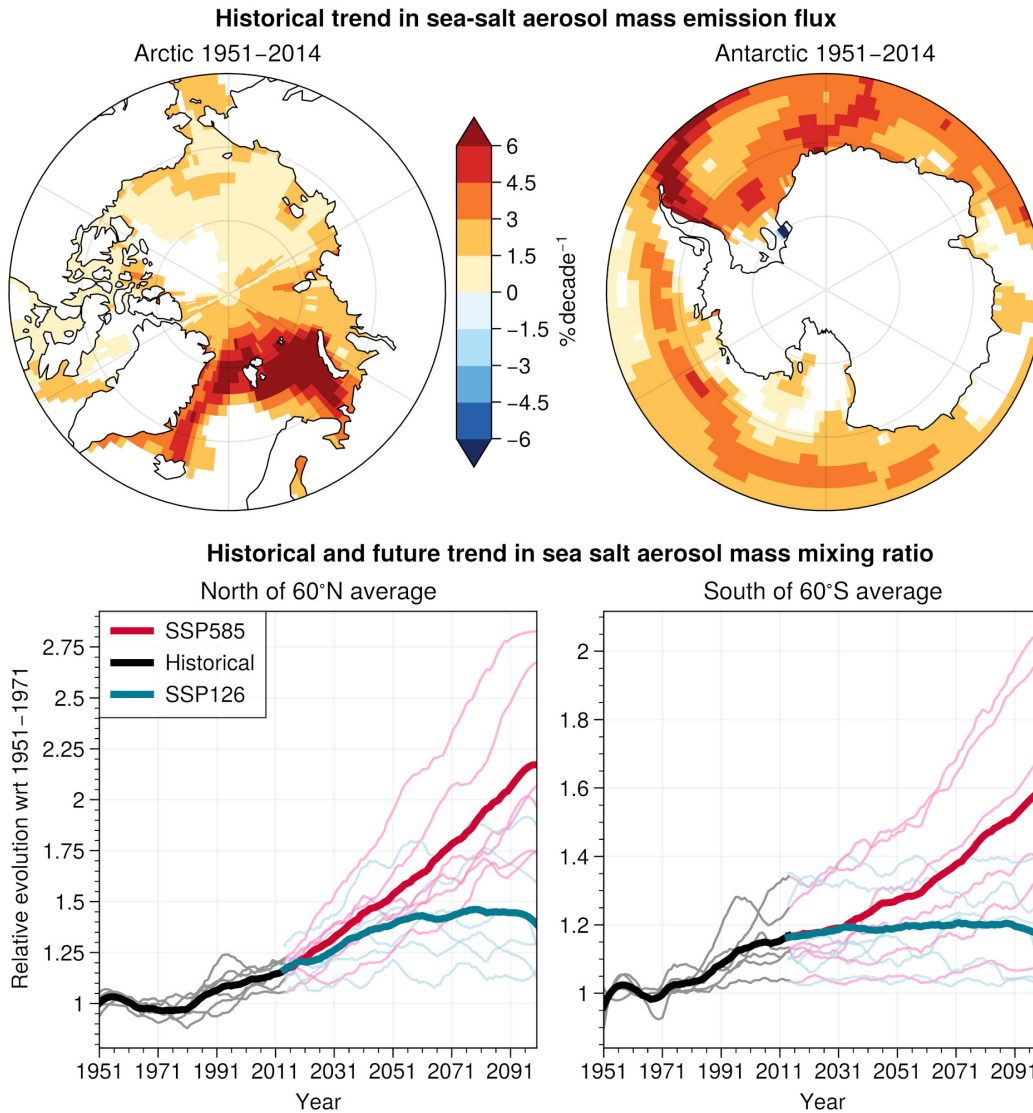




**Figure 9.** CMIP6 ensemble median and MODIS Terra (MOD08.M3) and Aqua (MYD08.M3) Dark Target/Deep Blue sea salt aerosol optical depth at 550 nm. Both MODIS data sets and CMIP6 model data are averages of monthly means for the period 2005–2014. The CMIP6 ensemble contains a subset of models providing the *od550ss* variable (BCC-ESM, EC-Earth, IPSL-CM6, MPI-ESM, MRI-ESM, NorESM). MODIS values are adjusted to only account for the contribution to AOD of particles with Angstrom exponent below 1. Right: average annual cycles of sea salt aerosol optical depth in MODIS (Terra in black, Aqua in grey - caps show one standard deviation) and CMIP6 models (orange). MODIS and CMIP6 values are collocated, i.e. CMIP6 values are used only for those grid cells where MODIS has valid records. Gray bars indicate, on an arbitrary scale common to both panels, the number of available records in MODIS Terra.



**Figure 10.** Change in top-of-the-atmosphere net downward radiative flux ( $rtmt$ ) in a scenario with doubled sea salt aerosol emissions under pre-industrial atmospheric composition (30 years under 1850 conditions). Stippling shows the grid points for which the difference between  $piClim-2xss$  and  $piClim-control$  is not significant at the 90% level according to a Wilcoxon test.

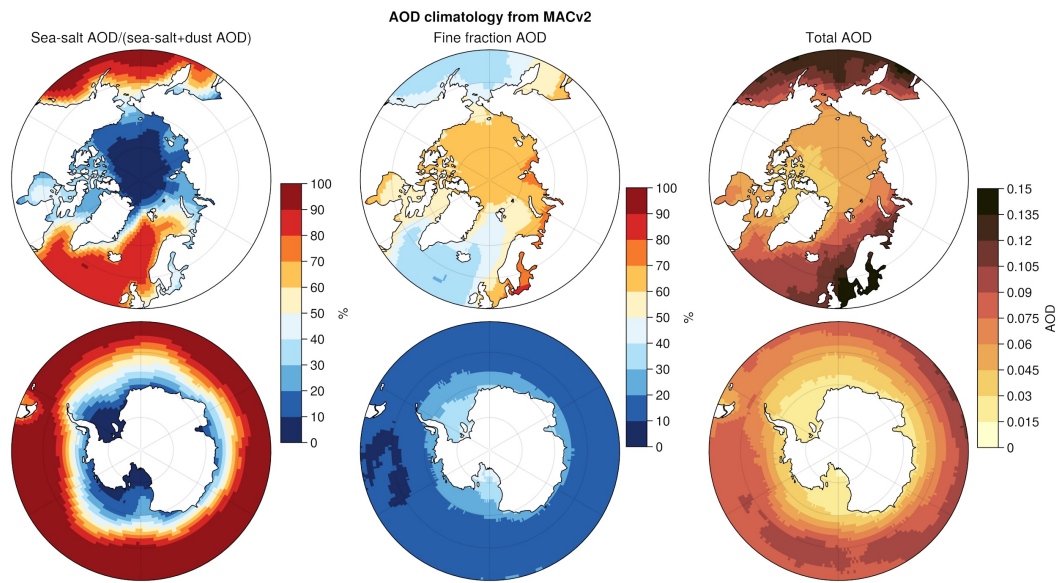


**Figure 11.** Top: trends in sea salt aerosol mass emissions in the ensemble mean for the period 1951–2014. The mass emission is normalized by the 1951–2014 average to obtain %/decade. Bottom: historical and future (relative to the 1951–1971 mean) yearly time series (1951–2099) of average sea salt surface mass mixing ratio north of 60°N (left) and south of 60°S (right), including ocean and land. Mixing ratios are weighted by grid cell area for spatial averaging. Time series are smoothed using a Savitzky-Golay filter with a window length of 19 years and a polynomial order 3. Ensemble means are shown as thicker lines (black for the historical period, blue for SSP126, red for SSP585). Individual members use the same color code but with thinner lines. Included models are: GISS, HadGEM, MIROC-ES2L, MRI-ESM, NorESM and UKESM. The smallest (largest, respectively) trend in SSP585 corresponds to NorESM (UKESM, respectively).

**Appendix A**

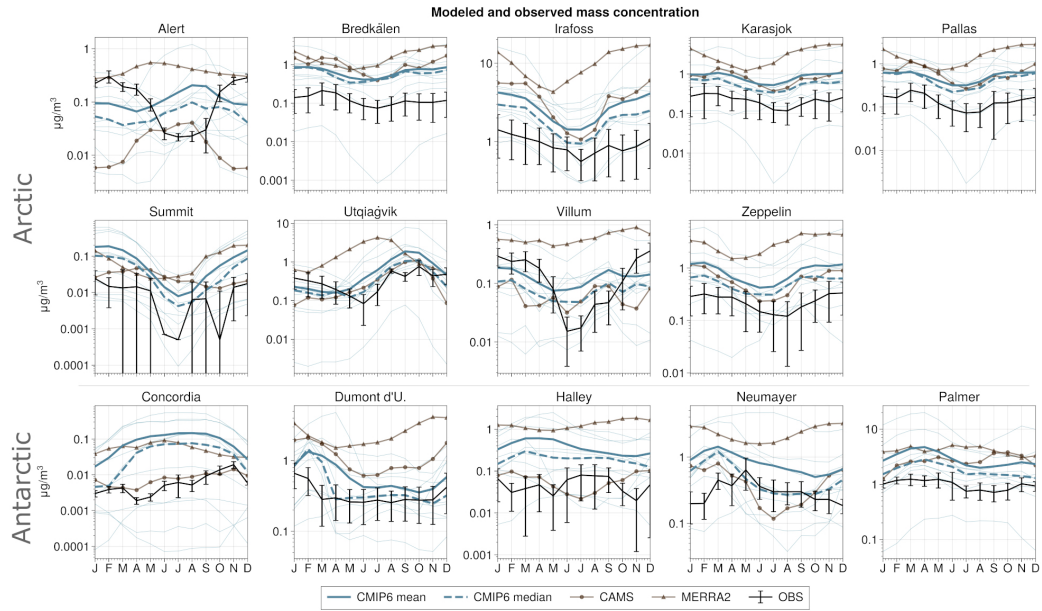
**Table A1.** Regionally averaged mean change in surface temperature (*tas* variable - °C) in the CMIP6 ensemble of models GISS, HadGEM, MIROC-ES2L, MRI-ESM, NorESM and UKESM. This change is computed as the difference between the 2000–2014 historical and 2085–2100 future averages. Arctic is all grid points north of 60°N, Antarctic is all grid points south of 60°S. Spread here refers to the difference between the model with largest increase and the model with smallest increase.

	Global		Arctic		Antarctic	
	Mean	Spread	Mean	Spread	Mean	Spread
SSP126	1.5	2.0	3.8	7.4	1.0	1.5
SSP585	5.1	3.8	10.8	10.0	4.5	3.1

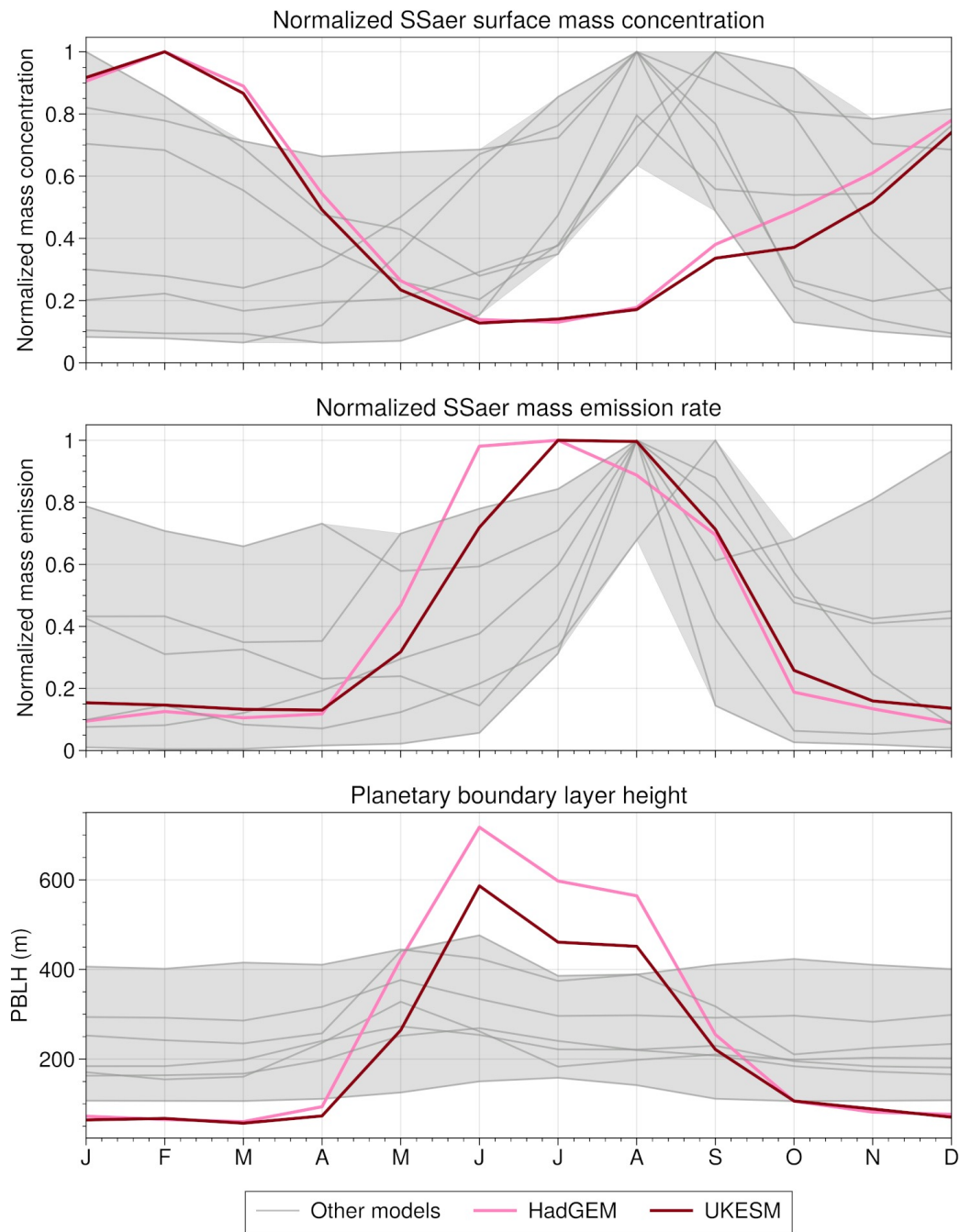
**A1 Sea salt dominance assessed from MACv2**

**Figure A1.** AOD characteristics at the poles from the MACv2 climatology (Kinne, 2019). Left: fraction of coarse AOD (dust+sea salt) attributed to sea salt (annual average climatology). Only dust and sea salt are considered here since we look at the coarse fraction AOD. Middle: fraction of total AOD from fine mode aerosols. Right: total AOD.

## A2 Non-normalized annual cycles versus observations



**Figure A2.** Annual cycle of sodium aerosol surface mass concentrations at 9 stations in the Arctic (top and middle) and 5 stations in the Antarctic (bottom). Observations are in black (caps show one standard deviation of monthly means), individual CMIP6 models (1951–2014) are in light blue, CMIP6 ensemble mean (solid line) and median (dashed line) is in darker blue, reanalyses (CAMS 2003–2021 - circles - and MERRA2 1980–2021 - triangles) are in brown.

**A3 Annual cycles at Alert**

**Figure A3.** Annual cycles of SSAer mass concentration (top - normalized), SSAer mass emission (middle - normalized) and boundary layer height (bottom) in CMIP6 at the grid point nearest to the Alert station. Average annual cycles for the period 1951–2014.

958

#### A4 Vertical distribution of SSaer and clouds

959

960

961

962

963

964

965

966

967

The evaluation conducted in Section 3.1 mainly focused on surface and column-integrated SSaer variables. To connect SSaer to clouds, information on the vertical distribution is needed. Figure A4 shows the regionally averaged profiles of  $m_{mrss}$  in the Arctic and Antarctic in the historical period, in Jun–Aug and Dec–Feb. This figure shows that the diversity at the surface affects also the vertical distribution. The inter-model spread is roughly constant from the surface up to 400 m altitude and remains above  $1 \mu\text{g g}^{-1}$  at 10 km altitude in winter months. Given that SSaer are injected high enough to interact with clouds (Figure A4), part of the diversity in cloud profiles at the poles could stem from this diversity in SSaer profile. In summer months, the profiles converge more rapidly.

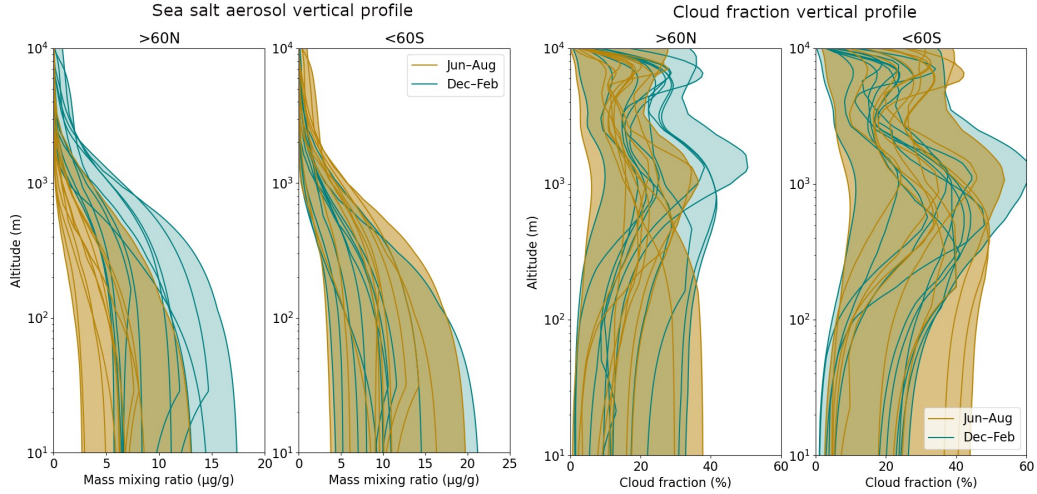


**Figure A4.** Left: Average vertical profile of sea salt aerosol mass mixing ratio in the Arctic (above  $60^\circ\text{N}$  - left) and Antarctic (below  $60^\circ\text{S}$  - right) in individual CMIP6 models, for Jun–Aug (blue) and Dec–Feb (yellow). Each line corresponds to one model, and the shaded area marks the ensemble envelope. Only grid points with less than 50% sea ice concentration are considered in this figure. Right: same as left but for cloud fraction. NB: the vertical axis is in logarithmic scale.



**A5** *piClim-2xss* scenario

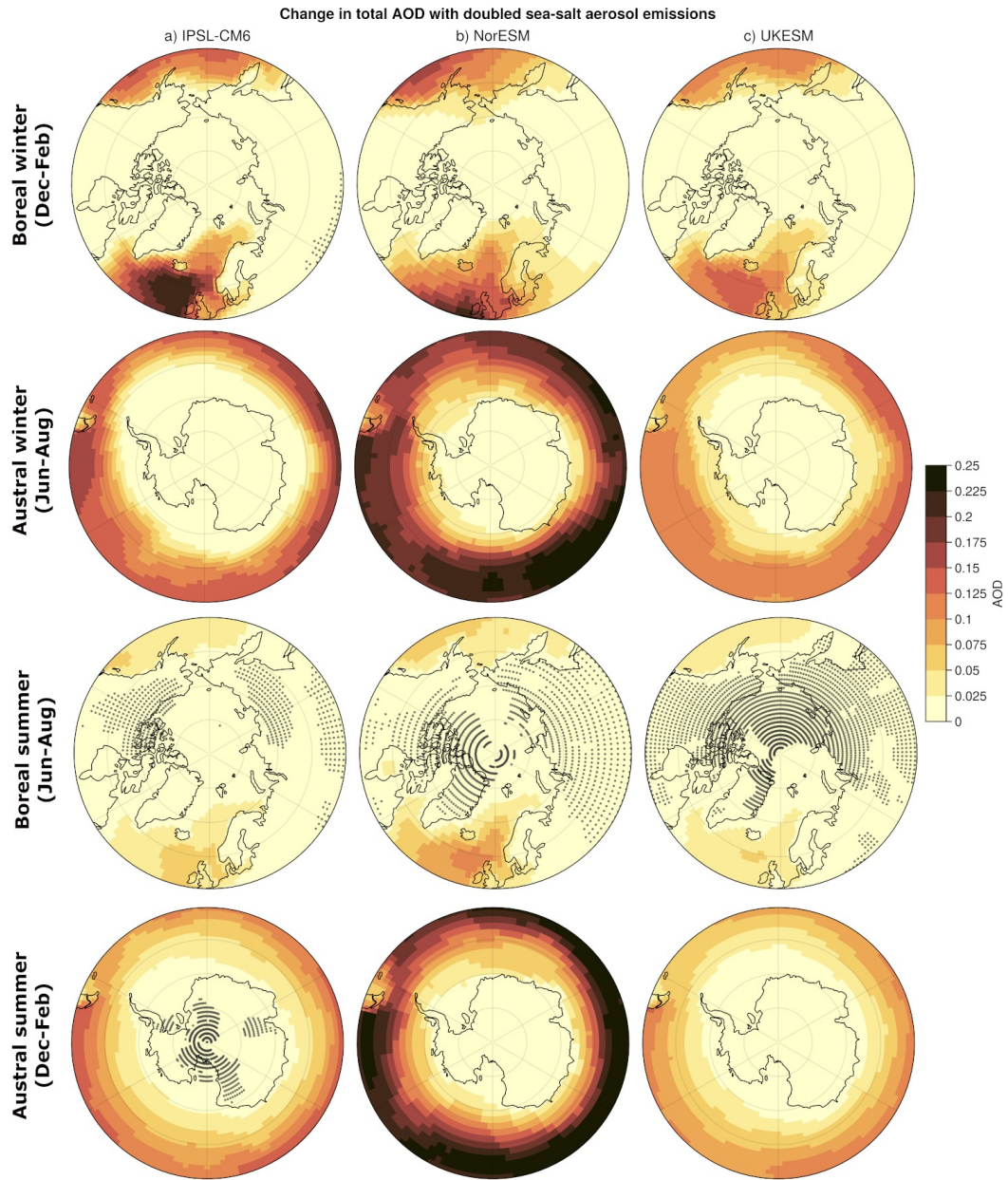


**Figure A5.** Same as Figure 10 but for total aerosol optical depth (*od550aer*).

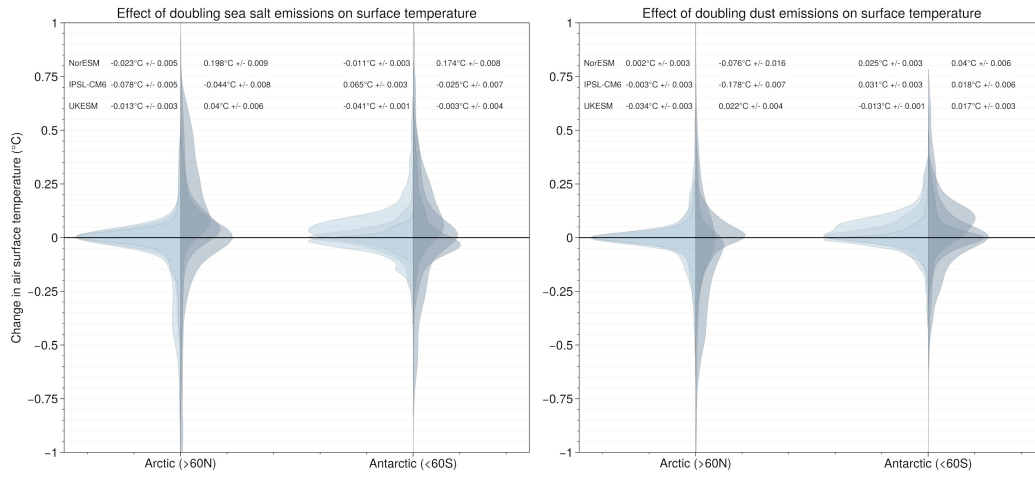


**Figure A6.** Difference in air surface temperature in the *piClim-control* and the *piClim-2xss* (left) and *piClim-2xdust* (right) experiments. Models included: IPSL-CM6, NorESM and UKESM. Summer is Jun–Aug in the Arctic, Dec–Feb in the Antarctic, and vice-versa. Values along the x-axis indicate the normalized frequency of temperature changes.

## A6 Drivers of sea salt emission trends

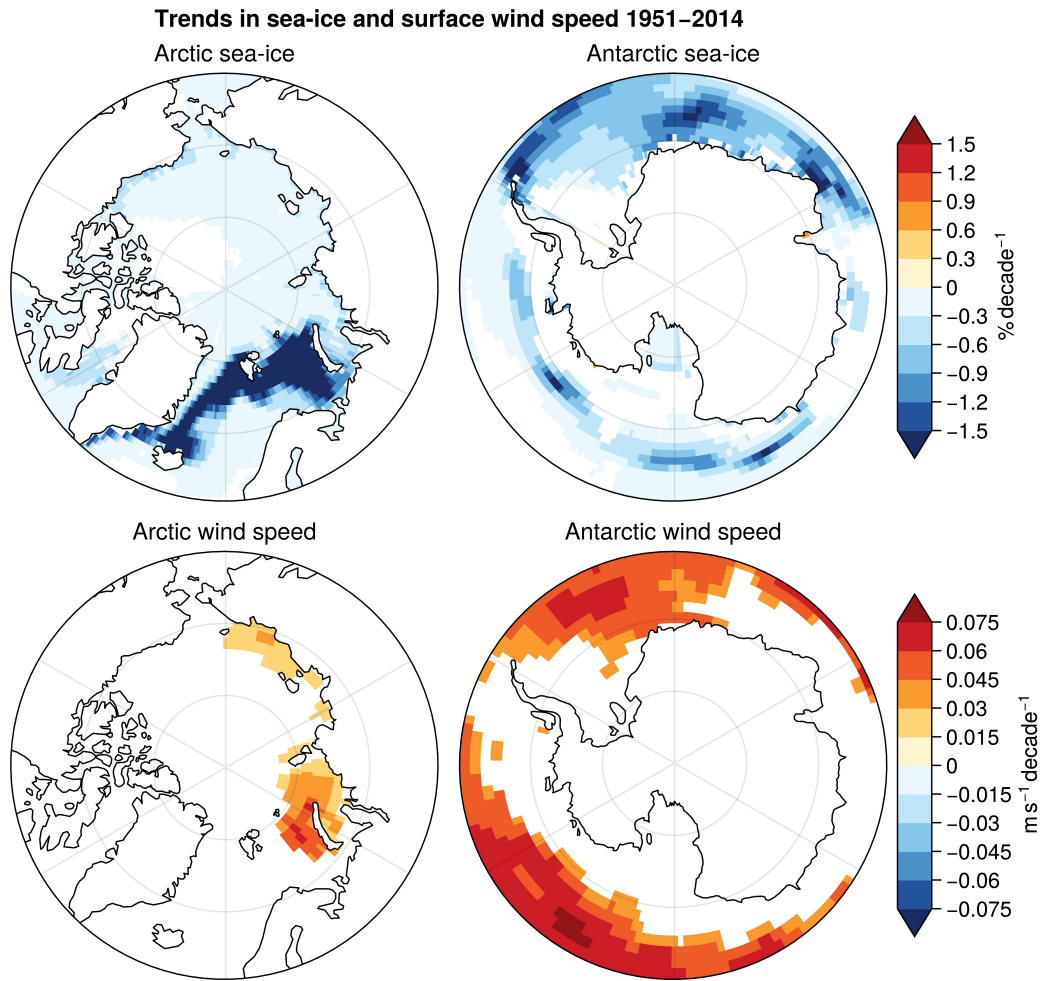


**Figure A7.** Historical trends in sea ice concentration (top) and surface wind speed (bottom) in CMIP6 models for the period 1951–2014. Included models are: GISS, HadGEM, MIROC-ES2L, MRI-ESM, NorESM and UKESM. Trends are computed following Mann-Kendall's test. Only significant trends at the 95% level are shown.

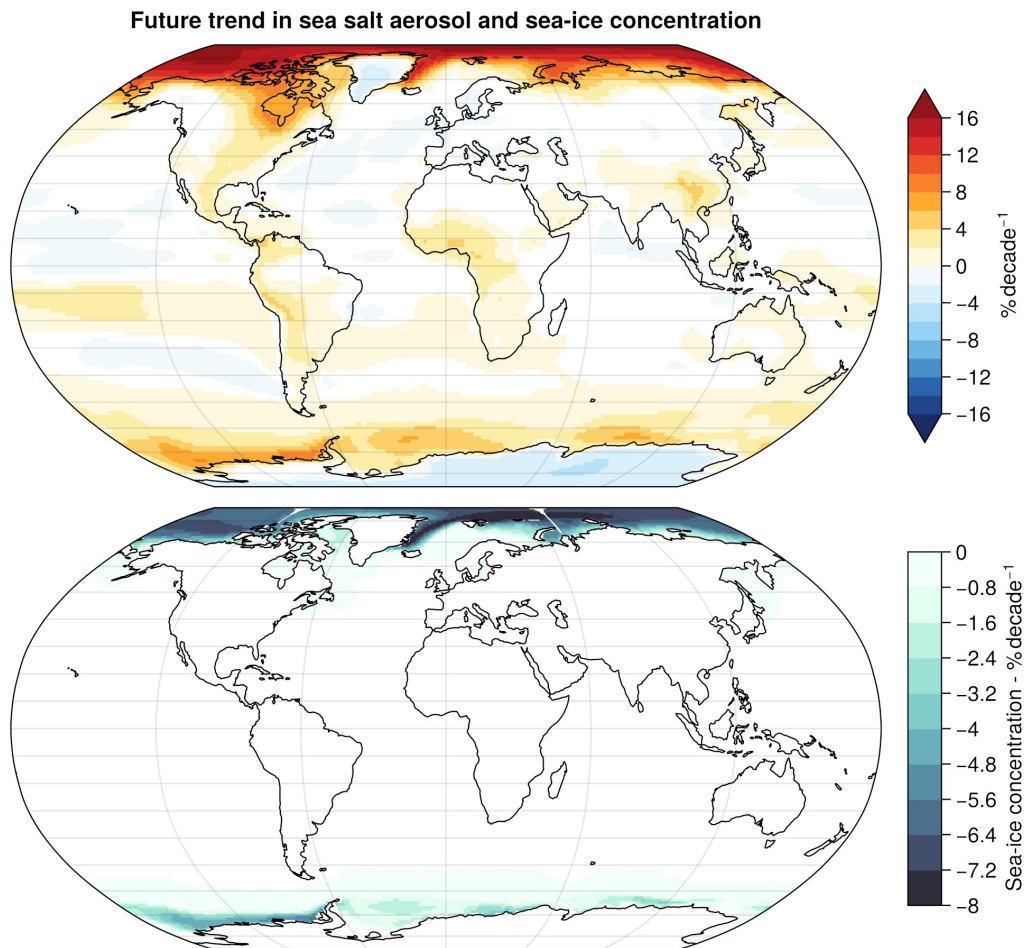


**Figure A8.** Maps of future trends in annual mean sea salt aerosol surface mass mixing ratio (top) and sea-ice concentration (bottom). Scenario SSP585. Multi-model mean from GISS, HadGEM, MIROC-ES2L, MRI-ESM, NorESM and UKESM.

## Open Research

The scripts used for computations and figure creation can be found at the following repository: [https://github.com/rlapere/CMIP6\\_SSA\\_Paper](https://github.com/rlapere/CMIP6_SSA_Paper)

## Author contributions

RL: Conceptualization, Methodology, Formal analysis, Investigation, Writing - Original Draft, Visualization. JT: Conceptualization, Methodology, Supervision, Writing - Original Draft. LM: Conceptualization, Methodology, Supervision, Writing - Review & Editing. MF, ML, BS, LS, XY, AE, RM, AR, MES, MS, PZ: Methodology, Writing - Review & Editing.

## Acknowledgments

This project has received funding from the European Union’s Horizon 2020 research and innovation programme under grant agreement No 101003826 via project CRiceS (Climate Relevant interactions and feedbacks: the key role of sea ice and Snow in the polar and global climate system). The authors also acknowledge the EU H2020 FORCeS project, contract No 821205. We also appreciate the effort of the CMIP6 modelling groups which contributed the data to the CMIP6 data archive. We acknowledge Yves Balkanski, Jean-Christophe Raut and Dirk Olivieé for the fruitful discussions.

## References

- Alkama, R., Taylor, P. C., Garcia-San Martin, L., Douville, H., Duveiller, G., Forzieri, G., ... Cescatti, A. (2020). Clouds damp the radiative impacts of polar sea ice loss. *The Cryosphere*, *14*, 2673–2686. doi: 10.5194/tc-14-2673-2020
- Allen, R. J., & Sherwood, S. C. (2011). The impact of natural versus anthropogenic aerosols on atmospheric circulation in the Community Atmosphere Model. *Climate Dynamics*, *36*, 1959–1978. doi: 10.1007/s00382-010-0898-8
- Andreae, M. O., & Rosenfeld, D. (2008). Aerosol–cloud–precipitation interactions. Part 1. The nature and sources of cloud-active aerosols. *Earth-Science Reviews*, *89*, 13–41. doi: 10.1016/j.earscirev.2008.03.001
- Atmoko, D., & Lin, T.-H. (2022). Sea Salt Aerosol Identification Based on Multispectral Optical Properties and Its Impact on Radiative Forcing over the Ocean. *Remote Sensing*, *14*, 3188. doi: 10.3390/rs14133188
- Bian, H., Froyd, K., Murphy, D. M., Dibb, J., Darmenov, A., Chin, M., ... Smirnov, A. (2019). Observationally constrained analysis of sea salt aerosol in the marine atmosphere. *Atmospheric Chemistry and Physics*, *19*, 10773–10785. doi: 10.5194/acp-19-10773-2019
- Boucher, O., Randall, D., Artaxo, P., Bretherton, C., Feingold, G., Forster, P., ... Zhang, X. Y. (2013). Climate Change 2013: The Physical Science Basis. Contribution of Working Group I to the Fifth Assessment Report of the Intergovernmental Panel on Climate Change [Stocker, T.F., D. Qin, G.-K. Plattner, M. Tignor, S.K. Allen, J. Boschung, A. Nauels, Y. Xia, V. Bex and P.M. Midgley (eds.)]. In (pp. 571–657). Cambridge University Press, Cambridge, UK and New York, NY, USA. doi: 10.1017/CBO9781107415324.016
- Boucher, O., Servonnat, J., Albright, A. L., Aumont, O., Balkanski, Y., Bastrikov, V., ... Vuichard, N. (2020). Presentation and Evaluation of the IPSL-CM6A-LR Climate Model. *Journal of Advances in Modeling Earth Systems*, *12*, e2019MS002010. doi: 10.1029/2019MS002010
- Browse, J., Carslaw, K. S., Mann, G. W., Birch, C. E., Arnold, S. R., & Leck, C. (2014). The complex response of Arctic aerosol to sea-ice retreat. *Atmospheric Chemistry and Physics*, *14*, 7543–7557. doi: 10.5194/acp-14-7543-2014

- 1018 Burgos, M. A., Andrews, E., Titos, G., Benedetti, A., Bian, H., Buchard, V., ...  
 1019 Zieger, P. (2020). A global model-measurement evaluation of particle light  
 1020 scattering coefficients at elevated relative humidity. *Atmospheric Chemistry*  
 1021 *and Physics*, *20*, 10231–10258. doi: 10.5194/acp-20-10231-2020
- 1022 Cai, Z., You, Q., Wu, F., Chen, H. W., Chen, D., & Cohen, J. (2021). Arctic Warm-  
 1023 ing Revealed by Multiple CMIP6 Models: Evaluation of Historical Simulations  
 1024 and Quantification of Future Projection Uncertainties. *Journal of Climate*, *34*,  
 1025 4871–4892. doi: 10.1175/JCLI-D-20-0791.1
- 1026 Chen, Y., Cheng, Y., Ma, N., Wei, C., Ran, L., Wolke, R., ... Wiedensohler, A.  
 1027 (2020). Natural sea-salt emissions moderate the climate forcing of anthro-  
 1028 pogenic nitrate. *Atmospheric Chemistry and Physics*, *20*, 771–786. doi:  
 1029 10.5194/acp-20-771-2020
- 1030 Curry, J. A., Schramm, J. L., Rossow, W. B., & Randall, D. (1996). Overview of  
 1031 Arctic Cloud and Radiation Characteristics. *Journal of Climate*, *9*, 1731–1764.  
 1032 doi: 10.1175/1520-0442(1996)009<1731:OOACAR>2.0.CO;2
- 1033 Dada, L., Angot, H., Beck, I., Baccarini, A., Quéléver, L. L. J., Boyer, M., ...  
 1034 Schmale, J. (2022). A central arctic extreme aerosol event triggered  
 1035 by a warm air-mass intrusion. *Nature Communications*, *13*, 1–15. doi:  
 1036 10.1038/s41467-022-32872-2
- 1037 Danabasoglu, G., Lamarque, J.-F., Bacmeister, J., Bailey, D. A., DuVivier, A. K.,  
 1038 Edwards, J., ... Strand, W. G. (2020). The Community Earth System Model  
 1039 Version 2 (CESM2). *Journal of Advances in Modeling Earth Systems*, *12*,  
 1040 e2019MS001916. doi: 10.1029/2019MS001916
- 1041 Dasarathy, S., Kar, J., Tackett, J., Rodier, S. D., Lu, X., Vaughan, M., ... Bow-  
 1042 man, J. S. (2021). Multi-Year Seasonal Trends in Sea Ice, Chlorophyll Con-  
 1043 centration, and Marine Aerosol Optical Depth in the Bellingshausen Sea.  
 1044 *Journal of Geophysical Research: Atmospheres*, *126*, e2021JD034737. doi:  
 1045 10.1029/2021JD034737
- 1046 DeMott, P. J., Hill, T. C. J., McCluskey, C. S., Prather, K. A., Collins, D. B., Sul-  
 1047 livan, R. C., ... Franc, G. D. (2016). Sea spray aerosol as a unique source  
 1048 of ice nucleating particles. *Proc Natl Acad Sci U S A*, *113*, 5797–5803. doi:  
 1049 10.1073/pnas.1514034112
- 1050 Diaconescu, E. P., Mailhot, A., Brown, R., & Chaumont, D. (2018). Evalua-  
 1051 tion of CORDEX-Arctic daily precipitation and temperature-based climate  
 1052 indices over Canadian Arctic land areas. *Clim Dyn*, *50*, 2061–2085. doi:  
 1053 10.1007/s00382-017-3736-4
- 1054 Dror, T., Lehahn, Y., Altaratz, O., & Koren, I. (2018). Temporal-Scale Anal-  
 1055 ysis of Environmental Controls on Sea Spray Aerosol Production Over the  
 1056 South Pacific Gyre. *Geophysical Research Letters*, *45*, 8637–8646. doi:  
 1057 10.1029/2018GL078707
- 1058 Döscher, R., Acosta, M., Alessandri, A., Anthoni, P., Arsouze, T., Bergman, T., ...  
 1059 Zhang, Q. (2022). The EC-Earth3 Earth system model for the Coupled Model  
 1060 Intercomparison Project 6. *Geoscientific Model Development*, *15*, 2973–3020.  
 1061 doi: 10.5194/gmd-15-2973-2022
- 1062 Eastman, R., & Warren, S. G. (2010). Interannual Variations of Arctic Cloud  
 1063 Types in Relation to Sea Ice. *Journal of Climate*, *23*, 4216–4232. doi:  
 1064 10.1175/2010JCLI3492.1
- 1065 ESGF. (2014). The Earth System Grid Federation: An open infrastructure for ac-  
 1066 cess to distributed geospatial data. *Future Gener. Comput. Syst*, *36*, 400–417.  
 1067 doi: 10.1016/j.future.2013.07.002
- 1068 Fanourgakis, G. S., Kanakidou, M., Nenes, A., Bauer, S. E., Bergman, T., Carslaw,  
 1069 K. S., ... Yu, F. (2019). Evaluation of global simulations of aerosol par-  
 1070 ticle and cloud condensation nuclei number, with implications for cloud  
 1071 droplet formation. *Atmospheric Chemistry and Physics*, *19*, 8591–8617. doi:  
 1072 10.5194/acp-19-8591-2019

- 1073 Flato, G., Marotzke, J., Abiodun, B., Braconnot, P., Chou, S. C., Collins, W., ...  
 1074 Rummukainen, M. (2013). Climate change 2013: The physical science basis.  
 1075 contribution of working group I to the fifth assessment report of the inter-  
 1076 governmental panel on climate change [stocker, t.f., d. Qin, G.-K. Plattner, M.  
 1077 Tignor, S.K. Allen, J. Boschung, A. Nauels, Y. Xia, V. Bex and P.M. Midgley (eds.)].  
 1078 In (pp. 741–882). Cambridge University Press, Cambridge, UK and New York,  
 1079 NY, USA. doi: 10.1017/CBO9781107415324.020
- 1080 Fossum, K. N., Ovadnevaite, J., Ceburnis, D., Dall’Osto, M., Marullo, S., Bellacicco,  
 1081 M., ... O’Dowd, C. (2018). Summertime Primary and Secondary Contribu-  
 1082 tions to Southern Ocean Cloud Condensation Nuclei. *Sci Rep*, *8*, 13844. doi:  
 1083 10.1038/s41598-018-32047-4
- 1084 Fossum, K. N., Ovadnevaite, J., Ceburnis, D., Preißler, J., Snider, J. R., Huang,  
 1085 R.-J., ... O’Dowd, C. (2020). Sea-spray regulates sulfate cloud droplet ac-  
 1086 tivation over oceans. *npj Climate and Atmospheric Science*, *3*, 1–6. doi:  
 1087 10.1038/s41612-020-0116-2
- 1088 Frey, M. M., Norris, S. J., Brooks, I. M., Anderson, P. S., Nishimura, K., Yang, X.,  
 1089 ... Wolff, E. W. (2020). First direct observation of sea salt aerosol production  
 1090 from blowing snow above sea ice. *Atmospheric Chemistry and Physics*, *20*,  
 1091 2549–2578. doi: 10.5194/acp-20-2549-2020
- 1092 Gliß, J., Mortier, A., Schulz, M., Andrews, E., Balkanski, Y., Bauer, S. E., ...  
 1093 Tsyro, S. G. (2021). AeroCom phase III multi-model evaluation of the aerosol  
 1094 life cycle and optical properties using ground- and space-based remote sensing  
 1095 as well as surface in situ observations. *Atmospheric Chemistry and Physics*,  
 1096 *21*, 87–128. doi: 10.5194/acp-21-87-2021
- 1097 Gong, S. L. (2003). A parameterization of sea-salt aerosol source function for sub-  
 1098 and super-micron particles. *Global Biogeochemical Cycles*, *17*. doi: 10.1029/  
 1099 2003GB002079
- 1100 Gryspeerdt, E., Goren, T., Sourdeval, O., Quaas, J., Mülmenstädt, J., Dipu, S.,  
 1101 ... Christensen, M. (2019). Constraining the aerosol influence on cloud liq-  
 1102 uid water path. *Atmospheric Chemistry and Physics*, *19*, 5331–5347. doi:  
 1103 10.5194/acp-19-5331-2019
- 1104 Grythe, H., Ström, J., Krejci, R., Quinn, P., & Stohl, A. (2014). A review of sea-  
 1105 spray aerosol source functions using a large global set of sea salt aerosol con-  
 1106 centration measurements. *Atmospheric Chemistry and Physics*, *14*, 1277–1297.  
 1107 doi: 10.5194/acp-14-1277-2014
- 1108 Gutjahr, O., Putrasahan, D., Lohmann, K., Jungclaus, J. H., von Storch, J.-S.,  
 1109 Bruggemann, N., ... Stössel, A. (2019). Max Planck Institute Earth Sys-  
 1110 tem Model (MPI-ESM1.2) for the High-Resolution Model Intercomparison  
 1111 Project (HighResMIP). *Geoscientific Model Development*, *12*, 3241–3281. doi:  
 1112 10.5194/gmd-12-3241-2019
- 1113 Hajima, T., Watanabe, M., Yamamoto, A., Tatebe, H., Noguchi, M. A., Abe, M., ...  
 1114 Kawamiya, M. (2020). Development of the MIROC-ES2L Earth system model  
 1115 and the evaluation of biogeochemical processes and feedbacks. *Geoscientific  
 1116 Model Development*, *13*, 2197–2244. doi: 10.5194/gmd-13-2197-2020
- 1117 Hall, A. (2004). The Role of Surface Albedo Feedback in Climate. *Journal of Cli-  
 1118 mate*, *17*, 1550–1568. doi: 10.1175/1520-0442(2004)017<1550:TROSAF>2.0.CO;  
 1119 2
- 1120 Hara, K., Osada, K., Yabuki, M., Takashima, H., Theys, N., & Yamanouchi,  
 1121 T. (2018). Important contributions of sea-salt aerosols to atmospheric  
 1122 bromine cycle in the Antarctic coasts. *Sci Rep*, *8*, 13852. doi: 10.1038/  
 1123 s41598-018-32287-4
- 1124 Held, A., Brooks, I. M., Leck, C., & Tjernström, M. (2011). On the potential  
 1125 contribution of open lead particle emissions to the central Arctic aerosol  
 1126 concentration. *Atmospheric Chemistry and Physics*, *11*, 3093–3105. doi:  
 1127 10.5194/acp-11-3093-2011

- 1128 Heslin-Rees, D., Burgos, M., Hansson, H.-C., Krejci, R., Ström, J., Tunved, P., &  
 1129 Zieger, P. (2020). From a polar to a marine environment: has the chang-  
 1130 ing Arctic led to a shift in aerosol light scattering properties? *Atmospheric*  
 1131 *Chemistry and Physics*, *20*, 13671–13686. doi: 10.5194/acp-20-13671-2020
- 1132 Holtslag, A. a. M., Svensson, G., Baas, P., Basu, S., Beare, B., Beljaars, A. C. M.,  
 1133 ... Wiel, B. J. H. V. D. (2013). Stable Atmospheric Boundary Lay-  
 1134 ers and Diurnal Cycles: Challenges for Weather and Climate Models.  
 1135 *Bulletin of the American Meteorological Society*, *94*, 1691–1706. doi:  
 1136 10.1175/BAMS-D-11-00187.1
- 1137 Huang, J., & Jaeglé, L. (2017). Wintertime enhancements of sea salt aerosol in  
 1138 polar regions consistent with a sea ice source from blowing snow. *Atmospheric*  
 1139 *Chemistry and Physics*, *17*, 3699–3712. doi: 10.5194/acp-17-3699-2017
- 1140 Huang, Y., Ding, Q., Dong, X., Xi, B., & Baxter, I. (2021). Summertime low clouds  
 1141 mediate the impact of the large-scale circulation on Arctic sea ice. *Commun*  
 1142 *Earth Environ*, *2*, 1–10. doi: 10.1038/s43247-021-00114-w
- 1143 Ioannidis, E., Law, K. S., Raut, J.-C., Marelle, L., Onishi, T., Kirpes, R. M., ...  
 1144 Pratt, K. A. (2022). *Modelling wintertime Arctic Haze and sea-spray aerosols*  
 1145 (Tech. Rep.). Aerosols/Atmospheric Modelling/Troposphere/Chemistry (chem-  
 1146 ical composition and reactions). doi: 10.5194/egusphere-2022-310
- 1147 Jaeglé, L., Quinn, P. K., Bates, T. S., Alexander, B., & Lin, J.-T. (2011). Global  
 1148 distribution of sea salt aerosols: new constraints from in situ and remote sens-  
 1149 ing observations. *Atmospheric Chemistry and Physics*, *11*, 3137–3157. doi:  
 1150 10.5194/acp-11-3137-2011
- 1151 Kinne, S. (2019). The MACv2 aerosol climatology. *Tellus B: Chemical and Physical*  
 1152 *Meteorology*, *71*, 1–21. doi: 10.1080/16000889.2019.1623639
- 1153 Kirpes, R. M., Bonanno, D., May, N. W., Fraund, M., Barget, A. J., Moffet, R. C.,  
 1154 ... Pratt, K. A. (2019). Wintertime Arctic Sea Spray Aerosol Composition  
 1155 Controlled by Sea Ice Lead Microbiology. *ACS Cent. Sci.*, *5*, 1760–1767. doi:  
 1156 10.1021/acscentsci.9b00541
- 1157 Korhonen, H., Carslaw, K. S., Forster, P. M., Mikkonen, S., Gordon, N. D., &  
 1158 Kokkola, H. (2010). Aerosol climate feedback due to decadal increases in  
 1159 Southern Hemisphere wind speeds. *Geophysical Research Letters*, *37*. doi:  
 1160 10.1029/2009GL041320
- 1161 Kramer, S. J., Alvarez, C., Barkley, A. E., Colarco, P. R., Custals, L., Delgado, L.,  
 1162 R., ... Zuidema, P. (2020). Apparent dust size discrepancy in aerosol reanal-  
 1163 ysis in north African dust after long-range transport. *Atmospheric Chemistry*  
 1164 *and Physics*, *20*, 10047–10062. doi: 10.5194/acp-20-10047-2020
- 1165 Lachlan-Cope, T. (2010). Antarctic clouds. *Polar Research*, *29*, 150–158. doi: 10  
 1166 .3402/polar.v29i2.6065
- 1167 Legrand, M., Yang, X., Preunkert, S., & Theys, N. (2016). Year-round records of sea  
 1168 salt, gaseous, and particulate inorganic bromine in the atmospheric boundary  
 1169 layer at coastal (Dumont d’Urville) and central (Concordia) East Antarctic  
 1170 sites. *Journal of Geophysical Research: Atmospheres*, *121*, 997–1023. doi:  
 1171 10.1002/2015JD024066
- 1172 Levine, J. G., Yang, X., Jones, A. E., & Wolff, E. W. (2014). Sea salt as an ice core  
 1173 proxy for past sea ice extent: A process-based model study. *Journal of Geo-*  
 1174 *physical Research: Atmospheres*, *119*, 5737–5756. doi: 10.1002/2013JD020925
- 1175 Li, S.-M., & Barrie, L. A. (1993). Biogenic sulfur aerosol in the Arctic troposphere:  
 1176 1. Contributions to total sulfate. *Journal of Geophysical Research: Atmo-*  
 1177 *spheres*, *98*, 20613–20622. doi: 10.1029/93JD02234
- 1178 Liu, S., Liu, C.-C., Froyd, K. D., Schill, G. P., Murphy, D. M., Bui, T. P., ... Gao,  
 1179 R.-S. (2021). Sea spray aerosol concentration modulated by sea surface tem-  
 1180 perature. *Proceedings of the National Academy of Sciences*, *118*, e2020583118.  
 1181 doi: 10.1073/pnas.2020583118
- 1182 Mahowald, N. M., Lamarque, J.-F., Tie, X. X., & Wolff, E. (2006). Sea-salt aerosol



- 1183 response to climate change: Last Glacial Maximum, preindustrial, and doubled  
 1184 carbon dioxide climates. *Journal of Geophysical Research: Atmospheres*, 111.  
 1185 doi: 10.1029/2005JD006459
- 1186 Manabe, S., & Wetherald, R. T. (1975). The Effects of Doubling the CO<sub>2</sub> Concen-  
 1187 tration on the climate of a General Circulation Model. *Journal of the Atmo-  
 1188 spheric Sciences*, 32, 3–15. doi: 10.1175/1520-0469(1975)032<0003:TEODTC>2  
 1189 .0.CO;2
- 1190 Mann, H. (1945). Nonparametric tests against trend. *Econometrica: Journal of the  
 1191 Econometric Society*, 245-259. doi: 10.2307/1907187
- 1192 Marelle, L., Thomas, J. L., Ahmed, S., Tuite, K., Stutz, J., Dommergue, A., ...  
 1193 Baladima, F. (2021). Implementation and Impacts of Surface and Blow-  
 1194 ing Snow Sources of Arctic Bromine Activation Within WRF-Chem 4.1.1.  
 1195 *Journal of Advances in Modeling Earth Systems*, 13, e2020MS002391. doi:  
 1196 10.1029/2020MS002391
- 1197 McCrystall, M. R., Stroeve, J., Serreze, M., Forbes, B. C., & Screen, J. A. (2021).  
 1198 New climate models reveal faster and larger increases in Arctic precipita-  
 1199 tion than previously projected. *Nature Communications*, 12, 6765. doi:  
 1200 10.1038/s41467-021-27031-y
- 1201 Mei, L., Xue, Y., de Leeuw, G., von Hoyningen-Huene, W., Kokhanovsky, A. A.,  
 1202 Istomina, L., ... Burrows, J. P. (2013). Aerosol optical depth retrieval in the  
 1203 Arctic region using MODIS data over snow. *Remote Sensing of Environment*,  
 1204 128, 234–245. doi: 10.1016/j.rse.2012.10.009
- 1205 Meinander, O., Dagsson-Waldhauserova, P., Amosov, P., Aseyeva, E., Atkins, C.,  
 1206 Baklanov, A., ... Vukovic Vimic, A. (2022). Newly identified climatically and  
 1207 environmentally significant high-latitude dust sources. *Atmospheric Chemistry  
 1208 and Physics*, 22, 11889–11930. doi: 10.5194/acp-22-11889-2022
- 1209 Meredith, M., Sommerkorn, M., Cassotta, S., Derksen, C., Ekaykin, A., Hollowed,  
 1210 A., ... Schuur, E. (2019). IPCC Special Report on the Ocean and Cryosphere  
 1211 in a Changing Climate [H.-O. Pörtner, D. C. Roberts, V. Masson-Delmotte,  
 1212 P. Zhai, M. Tignor, E. Poloczanska, K. Mintenbeck, A. Alegría, M. Nico-  
 1213 lai, A. Okem, J. Petzold, B. Rama, N. M. Weyer (eds.)]. In (p. 203-320).  
 1214 Cambridge University Press, Cambridge, UK and New York, NY, USA. doi:  
 1215 10.1017/9781009157964.005
- 1216 Miller, R. L., Schmidt, G. A., Nazarenko, L. S., Bauer, S. E., Kelley, M., Ruedy, R.,  
 1217 ... Yao, M.-S. (2021). CMIP6 Historical Simulations (1850–2014) With GISS-  
 1218 E2.1. *Journal of Advances in Modeling Earth Systems*, 13, e2019MS002034.  
 1219 doi: 10.1029/2019MS002034
- 1220 Monahan, E. C., Spiel, D. E., & Davidson, K. L. (1986). A Model of Marine  
 1221 Aerosol Generation Via Whitecaps and Wave Disruption. In E. C. Mon-  
 1222 ahan & G. M. Niocaill (Eds.), *Oceanic Whitecaps: And Their Role in  
 1223 Air-Sea Exchange Processes* (pp. 167–174). Springer Netherlands. doi:  
 1224 10.1007/978-94-009-4668-2\_16
- 1225 Mortier, A., Gliß, J., Schulz, M., Aas, W., Andrews, E., Bian, H., ... Tilmes, S.  
 1226 (2020). Evaluation of climate model aerosol trends with ground-based observa-  
 1227 tions over the last 2 decades – an AeroCom and CMIP6 analysis. *Atmospheric  
 1228 Chemistry and Physics*, 20, 13355–13378. doi: 10.5194/acp-20-13355-2020
- 1229 Murphy, D. M., Froyd, K. D., Bian, H., Brock, C. A., Dibb, J. E., DiGangi, J. P.,  
 1230 ... Yu, P. (2019). The distribution of sea-salt aerosol in the global tropo-  
 1231 sphere. *Atmospheric Chemistry and Physics*, 19, 4093–4104. doi:  
 1232 10.5194/acp-19-4093-2019
- 1233 Myhre, G., Shindell, D., Bréon, F.-M., Collins, W., Fuglestedt, J., Huang, J., ...  
 1234 Zhang, H. (2013). Climate Change 2013: The Physical Science Basis. Contri-  
 1235 bution of Working Group I to the Fifth Assessment Report of the Intergovern-  
 1236 mental Panel on Climate Change [Stocker, T.F., D. Qin, G.-K. Plattner, M.  
 1237 Tignor, S.K. Allen, J. Boschung, A. Nauels, Y. Xia, V. Bex and P.M. Midgley

- 1238 (eds.)). In (chap. Anthropogenic and Natural Radiative Forcing). Cambridge  
 1239 University Press, Cambridge, UK and New York, NY, USA.
- 1240 Mårtensson, E. M., Nilsson, E. D., de Leeuw, G., Cohen, L. H., & Hansson, H.-C.  
 1241 (2003). Laboratory simulations and parameterization of the primary marine  
 1242 aerosol production. *Journal of Geophysical Research: Atmospheres*, *108*. doi:  
 1243 10.1029/2002JD002263
- 1244 Nilsson, E. D., Rannik, U., Swietlicki, E., Leck, C., Aalto, P. P., Zhou, J., & Nor-  
 1245 man, M. (2001). Turbulent aerosol fluxes over the Arctic Ocean: 2. Wind-  
 1246 driven sources from the sea. *Journal of Geophysical Research: Atmospheres*,  
 1247 *106*, 32139–32154. doi: 10.1029/2000JD900747
- 1248 Norwegian Institute for Air Research. (2022). *Ebas*. Retrieved from [https://ebas](https://ebas.nilu.no/)  
 1249 [.nilu.no/](https://ebas.nilu.no/)
- 1250 Notz, D., & SIMIP Community. (2020). Arctic Sea Ice in CMIP6. *Geophysical Re-*  
 1251 *search Letters*, *47*, e2019GL086749. doi: 10.1029/2019GL086749
- 1252 O’Neill, B. C., Tebaldi, C., van Vuuren, D. P., Eyring, V., Friedlingstein, P., Hurtt,  
 1253 G., ... Sanderson, B. M. (2016). The Scenario Model Intercomparison Project  
 1254 (ScenarioMIP) for CMIP6. *Geoscientific Model Development*, *9*, 3461–3482.  
 1255 doi: 10.5194/gmd-9-3461-2016
- 1256 Palerme, C., Genthon, C., Claud, C., Kay, J. E., Wood, N. B., & L’Ecuyer, T.  
 1257 (2017). Evaluation of current and projected Antarctic precipitation in CMIP5  
 1258 models. *Climate Dynamics*, *48*, 225–239. doi: 10.1007/s00382-016-3071-1
- 1259 Platnick, S. (2015). *MODIS Atmosphere L3 Monthly Product*. (NASA MODIS  
 1260 Adaptive Processing System, Goddard Space Flight Center, USA. Ac-  
 1261 cess date: 20 July 2022, doi: 10.5067/MODIS/MOD08\_M3.006) doi:  
 1262 10.5067/MODIS/MOD08\\_M3.006
- 1263 Prank, M., Tonttila, J., Ahola, J., Kokkola, H., Kühn, T., Romakkaniemi, S., &  
 1264 Raatikainen, T. (2022). Impacts of marine organic emissions on low-level  
 1265 stratiform clouds – a large eddy simulator study. *Atmospheric Chemistry and*  
 1266 *Physics*, *22*, 10971–10992. doi: 10.5194/acp-22-10971-2022
- 1267 Qi, L., Li, Q., Li, Y., & He, C. (2017). Factors controlling black carbon distribu-  
 1268 tion in the Arctic. *Atmospheric Chemistry and Physics*, *17*, 1037–1059. doi: 10  
 1269 .5194/acp-17-1037-2017
- 1270 Quinn, P. K., Coffman, D. J., Johnson, J. E., Upchurch, L. M., & Bates, T. S.  
 1271 (2017). Small fraction of marine cloud condensation nuclei made up of sea  
 1272 spray aerosol. *Nature Geosci*, *10*, 674–679. doi: 10.1038/ngeo3003
- 1273 Quinn, P. K., Miller, T. L., Bates, T. S., Ogren, J. A., Andrews, E., & Shaw, G. E.  
 1274 (2002). A 3-year record of simultaneously measured aerosol chemical and  
 1275 optical properties at Barrow, Alaska. *Journal of Geophysical Research: Atmo-*  
 1276 *spheres*, *107*, 8–15. doi: 10.1029/2001JD001248
- 1277 Rantanen, M., Karpechko, A. Y., Lipponen, A., Nordling, K., Hyvärinen, O., Ru-  
 1278 ostenoja, K., ... Laaksonen, A. (2022). The Arctic has warmed nearly four  
 1279 times faster than the globe since 1979. *Commun Earth Environ*, *3*, 1–10. doi:  
 1280 10.1038/s43247-022-00498-3
- 1281 Regayre, L. A., Schmale, J., Johnson, J. S., Tatzelt, C., Baccarini, A., Henning, S.,  
 1282 ... Carslaw, K. S. (2020). The value of remote marine aerosol measurements  
 1283 for constraining radiative forcing uncertainty. *Atmospheric Chemistry and*  
 1284 *Physics*, *20*, 10063–10072. doi: 10.5194/acp-20-10063-2020
- 1285 Rhodes, R. H., Yang, X., & Wolff, E. W. (2018). Sea Ice Versus Storms: What  
 1286 Controls Sea Salt in Arctic Ice Cores? *Geophysical Research Letters*, *45*, 5572–  
 1287 5580. doi: 10.1029/2018GL077403
- 1288 Roach, L. A., Dörr, J., Holmes, C. R., Massonnet, F., Blockley, E. W., Notz, D., ...  
 1289 Bitz, C. M. (2020). Antarctic Sea Ice Area in CMIP6. *Geophysical Research*  
 1290 *Letters*, *47*, e2019GL086729. doi: 10.1029/2019GL086729
- 1291 Roussel, M.-L., Lemonnier, F., Genthon, C., & Krinner, G. (2020). Brief  
 1292 communication: Evaluating Antarctic precipitation in ERA5 and CMIP6

- 1293 against CloudSat observations. *The Cryosphere*, *14*, 2715–2727. doi:  
1294 10.5194/tc-14-2715-2020
- 1295 Salter, M. E., Zieger, P., Acosta Navarro, J. C., Grythe, H., Kirkevåg, A., Rosati,  
1296 B., ... Nilsson, E. D. (2015). An empirically derived inorganic sea spray  
1297 source function incorporating sea surface temperature. *Atmospheric Chemistry*  
1298 *and Physics*, *15*, 11047–11066. doi: 10.5194/acp-15-11047-2015
- 1299 Samset, B. H. (2022). Aerosol absorption has an underappreciated role in historical  
1300 precipitation change. *Communications Earth & Environment*, *3*, 1–8. doi: 10  
1301 .1038/s43247-022-00576-6
- 1302 Sand, M., Samset, B. H., Balkanski, Y., Bauer, S., Bellouin, N., Berntsen, T. K.,  
1303 ... Zhang, H. (2017). Aerosols at the poles: an AeroCom Phase II multi-  
1304 model evaluation. *Atmospheric Chemistry and Physics*, *17*, 12197–12218. doi:  
1305 10.5194/acp-17-12197-2017
- 1306 Sand, M., Samset, B. H., Myhre, G., Gliß, J., Bauer, S. E., Bian, H., ... Watson-  
1307 Parris, D. (2021). Aerosol absorption in global models from AeroCom  
1308 phase III. *Atmospheric Chemistry and Physics*, *21*, 15929–15947. doi:  
1309 10.5194/acp-21-15929-2021
- 1310 Satheesh, S. K., & Lubin, D. (2003). Short wave versus long wave radiative forcing  
1311 by Indian Ocean aerosols: Role of sea-surface winds. *Geophysical Research Let-*  
1312 *ters*, *30*. doi: 10.1029/2003GL017499
- 1313 Schmale, J., Zieger, P., & Ekman, A. M. L. (2021). Aerosols in current and future  
1314 Arctic climate. *Nat. Clim. Chang.*, *11*, 95–105. doi: 10.1038/s41558-020-00969  
1315 -5
- 1316 Schulzweida, U., Kornblueh, L., & Quast, R. (2012). *Climate Data Operators*  
1317 *User's Guide - Version 1.5.9* (Tech. Rep.). MPI for Meteorology, Brockmann  
1318 Consult.
- 1319 Seinfeld, J. H., & Pandis, S. N. (2016). *Atmospheric Chemistry and Physics: From*  
1320 *Air Pollution to Climate Change, 3rd Edition*. Wiley.
- 1321 Seland, O., Bentsen, M., Olivié, D., Toniazzo, T., Gjermundsen, A., Graff, L. S.,  
1322 ... Schulz, M. (2020). Overview of the Norwegian Earth System Model  
1323 (NorESM2) and key climate response of CMIP6 DECK, historical, and sce-  
1324 nario simulations. *Geoscientific Model Development*, *13*, 6165–6200. doi:  
1325 10.5194/gmd-13-6165-2020
- 1326 Sellar, A. A., Walton, J., Jones, C. G., Wood, R., Abraham, N. L., Andrejczuk, M.,  
1327 ... Griffiths, P. T. (2020). Implementation of U.K. Earth System Models for  
1328 CMIP6. *Journal of Advances in Modeling Earth Systems*, *12*, e2019MS001946.  
1329 doi: 10.1029/2019MS001946
- 1330 Smith, D. M., Screen, J. A., Deser, C., Cohen, J., Fyfe, J. C., García-Serrano, J., ...  
1331 Zhang, X. (2019). The Polar Amplification Model Intercomparison Project  
1332 (PAMIP) contribution to CMIP6: investigating the causes and consequences  
1333 of polar amplification. *Geoscientific Model Development*, *12*, 1139–1164. doi:  
1334 10.5194/gmd-12-1139-2019
- 1335 Smith, M. H., & Harrison, N. M. (1998). The sea spray generation function. *Journal*  
1336 *of Aerosol Science*, *29*, S189–S190. doi: 10.1016/S0021-8502(98)00280-8
- 1337 Sogacheva, L., Popp, T., Sayer, A. M., Dubovik, O., Garay, M. J., Heckel, A., ...  
1338 Arola, A. (2020). Merging regional and global aerosol optical depth records  
1339 from major available satellite products. *Atmospheric Chemistry and Physics*,  
1340 *20*, 2031–2056. doi: 10.5194/acp-20-2031-2020
- 1341 Struthers, H., Ekman, A. M. L., Glantz, P., Iversen, T., Kirkevåg, A., Seland, O.,  
1342 ... Nilsson, E. D. (2013). Climate-induced changes in sea salt aerosol number  
1343 emissions: 1870 to 2100. *Journal of Geophysical Research: Atmospheres*, *118*,  
1344 670–682. doi: 10.1002/jgrd.50129
- 1345 Struthers, H., Ekman, A. M. L., Glantz, P., Iversen, T., Kirkevåg, A., Mårtensson,  
1346 E. M., ... Nilsson, E. D. (2011). The effect of sea ice loss on sea salt aerosol  
1347 concentrations and the radiative balance in the Arctic. *Atmospheric Chemistry*

- 1348 *and Physics*, *11*, 3459–3477. doi: 10.5194/acp-11-3459-2011
- 1349 Stuecker, M. F., Bitz, C. M., Armour, K. C., Proistosescu, C., Kang, S. M.,  
 1350 Xie, S.-P., . . . Jin, F.-F. (2018). Polar amplification dominated by lo-  
 1351 cal forcing and feedbacks. *Nature Climate Change*, *8*, 1076–1081. doi:  
 1352 10.1038/s41558-018-0339-y
- 1353 Séférian, R., Nabat, P., Michou, M., Saint-Martin, D., Voldoire, A., Colin, J., . . .  
 1354 Madec, G. (2019). Evaluation of CNRM Earth System Model, CNRM-ESM2-  
 1355 1: Role of Earth System Processes in Present-Day and Future Climate. *J. Adv.*  
 1356 *Model. Earth Syst.*, *11*, 4182–4227. doi: 10.1029/2019MS001791
- 1357 Takemura, T., Nakajima, T., Dubovik, O., Holben, B. N., & Kinne, S. (2002).  
 1358 Single-Scattering Albedo and Radiative Forcing of Various Aerosol Species  
 1359 with a Global Three-Dimensional Model. *Journal of Climate*, *15*, 333–352.  
 1360 doi: 10.1175/1520-0442(2002)015(0333:SSAARF)2.0.CO;2
- 1361 Tang, M. S. Y., Chenoli, S. N., Samah, A. A., & Hai, O. S. (2018). An as-  
 1362 sessment of historical Antarctic precipitation and temperature trend us-  
 1363 ing CMIP5 models and reanalysis datasets. *Polar Science*, *15*, 1–12. doi:  
 1364 10.1016/j.polar.2018.01.001
- 1365 Tewari, K., Mishra, S. K., Salunke, P., & Dewan, A. (2022). Future projections of  
 1366 temperature and precipitation for Antarctica. *Environmental Research Letters*,  
 1367 *17*, 014029. doi: 10.1088/1748-9326/ac43e2
- 1368 Thornhill, G., Collins, W., Olivie, D., Skeie, R. B., Archibald, A., Bauer, S., . . .  
 1369 Weber, J. (2021). Climate-driven chemistry and aerosol feedbacks in CMIP6  
 1370 Earth system models. *Atmospheric Chemistry and Physics*, *21*, 1105–1126.  
 1371 doi: 10.5194/acp-21-1105-2021
- 1372 Tunved, P., Ström, J., & Krejci, R. (2013). Arctic aerosol life cycle: linking aerosol  
 1373 size distributions observed between 2000 and 2010 with air mass transport  
 1374 and precipitation at Zeppelin station, Ny-Ålesund, Svalbard. *Atmospheric*  
 1375 *Chemistry and Physics*, *13*, 3643–3660. doi: 10.5194/acp-13-3643-2013
- 1376 Turner, J., Comiso, J. C., Marshall, G. J., Lachlan-Cope, T. A., Bracegirdle, T.,  
 1377 Maksym, T., . . . Orr, A. (2009). Non-annular atmospheric circulation  
 1378 change induced by stratospheric ozone depletion and its role in the recent  
 1379 increase of Antarctic sea ice extent. *Geophysical Research Letters*, *36*. doi:  
 1380 10.1029/2009GL037524
- 1381 Vavrus, S. J., & Alkama, R. (2022). Future trends of arctic surface wind speeds and  
 1382 their relationship with sea ice in CMIP5 climate model simulations. *Clim Dyn*,  
 1383 *59*, 1833–1848. doi: 10.1007/s00382-021-06071-6
- 1384 Wilson, T. W., Ladino, L. A., Alpert, P. A., Breckels, M. N., Brooks, I. M., Browse,  
 1385 J., . . . Murray, B. J. (2015). A marine biogenic source of atmospheric ice-  
 1386 nucleating particles. *Nature*, *525*, 234–238. doi: 10.1038/nature14986
- 1387 Wu, T., Zhang, F., Zhang, J., Jie, W., Zhang, Y., Wu, F., . . . Hu, A. (2020). Beijing  
 1388 Climate Center Earth System Model version 1 (BCC-ESM1): model descrip-  
 1389 tion and evaluation of aerosol simulations. *Geoscientific Model Development*,  
 1390 *13*, 977–1005. doi: 10.5194/gmd-13-977-2020
- 1391 Xian, P., Zhang, J., O’Neill, N. T., Toth, T. D., Sorenson, B., Colarco, P. R., . . .  
 1392 Ranjbar, K. (2022). Arctic spring and summertime aerosol optical depth  
 1393 baseline from long-term observations and model reanalyses – Part 1: Clima-  
 1394 tology and trend. *Atmospheric Chemistry and Physics*, *22*, 9915–9947. doi:  
 1395 10.5194/acp-22-9915-2022
- 1396 Xu, W., Ovadnevaite, J., Fossom, K. N., Lin, C., Huang, R.-J., Ceburnis, D., &  
 1397 O’Dowd, C. (2022). Sea spray as an obscured source for marine cloud nuclei.  
 1398 *Nat. Geosci.*, *15*, 282–286. doi: 10.1038/s41561-022-00917-2
- 1399 Yang, X., Frey, M. M., Rhodes, R. H., Norris, S. J., Brooks, I. M., Anderson, P. S.,  
 1400 . . . Wolff, E. W. (2019). Sea salt aerosol production via sublimating wind-  
 1401 blown saline snow particles over sea ice: parameterizations and relevant micro-  
 1402 physical mechanisms. *Atmospheric Chemistry and Physics*, *19*, 8407–8424. doi:

- 1403 10.5194/acp-19-8407-2019  
1404 Yang, X., Pyle, J. A., & Cox, R. A. (2008). Sea salt aerosol production and bromine  
1405 release: Role of snow on sea ice. *Geophysical Research Letters*, *35*. doi: 10  
1406 .1029/2008GL034536
- 1407 Yukimoto, S., Kawai, H., Koshiro, T., Oshima, N., Yoshida, K., Urakawa, S., ...  
1408 Ishii, M. (2019). The Meteorological Research Institute Earth System Model  
1409 Version 2.0, MRI-ESM2.0: Description and Basic Evaluation of the Physical  
1410 Component. *Journal of the Meteorological Society of Japan*, *97*, 931–965. doi:  
1411 10.2151/jmsj.2019-051
- 1412 Zhu, L., Jacob, D. J., Eastham, S. D., Sulprizio, M. P., Wang, X., Sherwen, T., ...  
1413 Percival, C. J. (2019). Effect of sea salt aerosol on tropospheric bromine  
1414 chemistry. *Atmospheric Chemistry and Physics*, *19*, 6497–6507. doi:  
1415 10.5194/acp-19-6497-2019
- 1416 Zieger, P., Väisänen, O., Corbin, J. C., Partridge, D. G., Bastelberger, S., Mousavi-  
1417 Fard, M., ... Salter, M. E. (2017). Revising the hygroscopicity of inorganic sea  
1418 salt particles. *Nature Communications*, *8*, 15883. doi: 10.1038/ncomms15883
- 1419 Zinke, J., Nilsson, E. D., Zieger, P., & Salter, M. E. (2022). The Effect of Seawa-  
1420 ter Salinity and Seawater Temperature on Sea Salt Aerosol Production. *Jour-  
1421 nal of Geophysical Research: Atmospheres*, *127*, e2021JD036005. doi: 10.1029/  
1422 2021JD036005
- 1423 Zábori, J., Krejci, R., Ekman, A. M. L., Mårtensson, E. M., Ström, J., de Leeuw,  
1424 G., & Nilsson, E. D. (2012). Wintertime Arctic Ocean sea water proper-  
1425 ties and primary marine aerosol concentrations. *Atmospheric Chemistry and  
1426 Physics*, *12*, 10405–10421. doi: 10.5194/acp-12-10405-2012